High-resolution sea surface salinity maps in coastal seas based on geostationary ocean color images: Quantitative analysis of river-plume dynamics

[Author & co-authors]
Satoshi NAKADA[1]: Email: nakada.satoshi.2w@kyoto-u.ac.jp
Shiho KOBAYASHI[2]: Email: shihok@kais.kyoto-u.ac.jp
Masataka HAYASHI[3]: Email: m-hayashi@sat-gis.co.jp
Joji ISHIZAKA[4]: Email: jishizaka@nagoya-u.jp
Satoshi AKIYAMA[5]: Email: AkiyamaS@o-suishi.zaqrs.jp
Masaki FUCHI[6]: Email: mfuchi@maritime.kobe-u.ac.jp
Masaki NAKAJIMA[5]: Email: NakajimaM@o-suishi.zaqrs.jp

[Institutional addresses]
1 Graduate School of Maritime Science, Kobe University, 5-1-1 Fukae-minami, Higashi-nada-ku, Kobe, Japan 658-0022.
2 Field Science Education and Research Center, Kyoto University, Kitashirakawa -Oiwake Cho, Sakyo-ku, Kyoto, Japan 606-8502.
3 Science and Technology Co., Ltd., 3-9-2, Kobai-cho, Showa-ku, Nagoya-shi, Aichi, Japan 466-0031.
4 Division for Land-Ocean Ecosystem Research Institute for Space-Earth Environmental Research (ISEE), Nagoya University, Furo-cho, Chikusa-ku, Nagoya, Japan 464-8601.
5 Research Institute of Environment, Agriculture and Fisheries, Osaka Prefecture, 2926-1 Tanigawa, Tanagawa, Misaki-cho, Sennan-gun, Osaka, Japan, 599-0311
6 International Maritime Research Centre, Kobe University, Kobe, Japan, 5-1-1 Fukae-minami, Higashi-nada-ku, Kobe, Japan 658-0022.

***Corresponding author: Satoshi Nakada**
TEL: +81-78-431-6252 **FAX:** +81-78-431-6366
e-mail: snakada@maritime.kobe-u.ac.jp

Running title: Development of surface salinity maps in coastal oceans.

Abstract

Sea-surface salinity (SSS) in coastal oceans is a direct indicator of riverine plumes and provides essential information about the ocean environment and ecosystem, which affects coastal fisheries, aquaculture, and marine harvests. However, to accurately capture SSS patterns in coastal oceans, high temporal and spatial resolutions are required. This paper introduces a methodology to produce high-resolution (~500 m) SSS maps for analysis of river plumes in coastal oceans based on hourly chromophoric dissolved organic matter (CDOM) data collected by the Geostationary Ocean Color Imager (GOCI). Osaka Bay, located in the eastern Seto Inland Sea, was selected as a pilot region. A comparison between the initial estimates and calibrated SSS data showed a substantial decrease in estimation error, by up to 71%, over a wide range of salinity (20–34) using *in situ* SSS data collected through an automated observation system. Calculating the salinity anomaly based on the SSS map to identify plume areas, we evaluated the impact of a large runoff event induced by a super typhoon on the river plumes. After the plume formed in the estuary, it extended southward to the bay mouth along the southeastern coast. The plume area during the post-typhoon period covered half of the bay, approximately 1.5 times the area during the pre-typhoon period. The post-typhoon low SSS period continued for approximately two weeks. Our approach can be of practical use for analyzing the dynamics of river plumes in coastal oceans, leading to the development of coastal ocean prediction models related to operational oceanography.

Keywords: Sea-surface salinity, coastal oceans, chromophoric dissolved organic matter, river plume, typhoon, Geostationary ocean color satellite, Osaka Bay

1. Introduction

Riverine freshwater plumes in coastal oceans are crucial contributors to deposition, re-suspension, and transport of dissolved materials such as land-derived nutrients (e.g., Herbeck et al., 2011; Fichot et al., 2014). The riverine materials input to regions of freshwater influence (ROFI), which exist between oceans and estuaries (Simpson, 1997), often yield significant fishery resources and may be associated with eutrophication in the river plume. The plume, which is characterized by low-salinity water from the estuary, can determine the water density structure and circulation system of these regions (Garvine, 1999). Sea-surface salinity (SSS) is a direct indicator of a freshwater plume associated with river discharge (Sasaki et al., 2008). Therefore, accurate SSS maps are essential to investigations of the ocean environment and ecosystems relevant to coastal fisheries, aquaculture, and marine harvests. This paper addresses the establishment of spatiotemporally high-resolution SSS maps to accurately analyze river plumes in coastal oceans based on ocean color products of geostationary satellites.

High-resolution SSS maps are urgently needed in marginal and coastal oceans to meet growing scientific and societal demands. For example, the low salinity water formed by the Changjiang (Yangtze) River discharge is used as an index to predict the abundance of giant jellyfish (*Nemopilema nomurai*), thus affecting the efficiency of fishery operations (Kawahara et al., 2006). The abundance of these jellyfish is strongly correlated with riverine SSS along the coastal branch of the Tsushima Warm Current (Senjyu et al., 2013). In Funka Bay, Japan, located in the subarctic Oyashio region, the river plume contains abundant nutrients from snowmelt runoff that can increase the biomass of phytoplankton associated with scallop fishery production (Nakada et al., 2014). Thus, SSS data can provide a practical index for aquaculture and fisheries, and holds similar significance for nori (*Porphyra*) production and discoloration in the Seto Inland Sea, Japan (e.g. Takagi et al., 2012), and the distribution, survival, and growth of commercial fishery resources such as oysters in the Chesapeake Bay, United States (Vogel and Brown 2016). From an oceanographic standpoint, SSS is primarily useful for detection of ocean currents and water masses, such as the East Sakhalin Current (Kuroda et al., 2013) and Coastal Oyashio Water in summer (Kusaka et al., 2013). SSS can be a representative indicator for hydrological factors, such as riverine freshwater input to the ocean associated with river plumes (e.g., Son et al., 2012) and evaporation and precipitation over the ocean (Lagerloef et al., 2008). In numerical and modeling studies, SSS can be used as input data to determine the surface boundary and initial conditions, in addition to validation data for simulated SSS in an urbanized nearshore area with numerous landfills (Nakada et al., 2017). In particular, high-resolution SSS maps of the coastal oceans are essential for validating the SSS simulated by high-resolution coastal ocean models to improve model reproducibility (Nakada et al., 2012; Urakawa et al., 2015; Sakamoto et al., 2016).

To date, satellite-derived SSS datasets or maps have been established with global coverage based on microwave measurements (L-band radiometers), such as the Soil Moisture and Ocean Salinity (SMOS, European Space Agency, ESA) and Aquarius/SAC-D (National Aeronautics and Space

Administration, NASA) missions to directly monitor salinity at the ocean surface (e.g., Lagerloef et al., 2008). Satellite-derived SSS data from current microwave sensors remains a limitation, as they cannot produce satisfactory resolution in coastal oceans (Bai et al., 2013) due to land contamination, coarse spatial resolution (typically 30–300 km), and long revisiting time (3 days or more) (Koblinsky et al., 2003; Lagerloef et al., 2008; Font et al., 2010; Kerr et al., 2010). Neither mission was designed to observe SSS accurately in coastal regions with sufficient spatial and temporal resolution to monitor river plumes, because the SSS associated with a riverine plume exhibits high variation at small temporal and spatial scales. For example, the SSS distribution difference between pre- and post-typhoon samples can vary considerably due to the large amount of river runoff (Herbeck et al., 2011).

To estimate SSS with high resolution in coastal seas, two approaches employing satellite ocean color products can be used. Recent approaches directly apply ocean color data based on the neural networks method (Geiger et al., 2013), and utilize remote sensing reflectance data based on multiple statistical models (Urquhart et al., 2012, Qing et al. 2013). For these studies, use of satellite ocean color data in coastal areas can be prone to error due to the presence of multiple suspended constituents, including biogenic and terrigenous particles such as phytoplankton (Vogel and Brown, 2016); salinity estimated using those approaches is necessary for *in situ* ocean color datasets, such as remote sensing reflectance, to sea truth with appropriate spatial and temporal resolution.

The most frequently used approach is to utilize the linear relationship between SSS and the optical absorption coefficient of colored (or chromophoric) dissolved organic matter (a_{CDOM}), which has a significant negative correlation (e.g., Binding and Bowers, 2003; Wouthuyzen et al., 2011). Chromophoric dissolved organic matter (CDOM) is soluble in riverine freshwater and rich in terrestrial plant-derived compounds but is made mostly of biologically recalcitrant substances (Hansell, 2013). Therefore, CDOM can behave conservatively in estuaries or ROFIs, where physical mixing prevails (Bowers and Brett, 2008). In recent years, SSS has been empirically estimated from satellite-derived a_{CDOM} data based on the SSS–CDOM relationship in many river-plume dominated oceans, such as the outputs of the Amazon and Orinoco Rivers (e.g., Hu et al., 2004; Del Vecchio and Subramaniam, 2004; Molleri et al., 2010), the Changjiang River (e.g., Sasaki et al., 2008; Bai et al., 2014), and the Mississippi River (Del Castillo and Miller, 2008). However, these studies were based on daily satellite data and were limited to large ocean regions (~10^5 km^2) relative to the horizontal resolution (~1 km) of ocean color sensors such as NASA's Moderate Resolution Imaging Spectroradiometer (MODIS). In the coastal oceans, higher-resolution data are necessary to study oceanic phenomena that fluctuate in time and space, which are also difficult to elucidate using limited field surveys (Vogel and Brown, 2016).

The Korean geostationary satellite Communication, Ocean and Meteorological Satellite (COMS), delivered by the Ariane 5 launch vehicle, was successfully launched in June 2010 from the Space Center in Kourou, French Guiana. The COMS carries the world's first geostationary ocean color sensor, the Geostationary Ocean Color Imager (GOCI) to measure radiance from the ocean surface in the

visible and near-infrared bands. Observations from GOCI-COMS are available to easily derive high-resolution (~500 m) a_{CDOM} data, in addition to the higher temporal resolution (hourly) in daytime hours. These specifications are advantageous to observation of ocean color compared with other sensors.

This paper presents a novel methodology to produce high-resolution SSS maps based on GOCI products at the local scale (~10^3 km^3) in a semi-enclosed bay over a long-term period. Furthermore, this method can improve accuracy of SSS estimates by utilizing real-time *in situ* SSS data from an automated observation system. In this research, we first evaluated how this methodology can improve the accuracy of SSS datasets in conjunction with time series of hourly *in situ* SSS data. Then, SSS maps with high spatiotemporal resolution were produced to analyze seasonal SSS patterns and to quantify the river plume area. Finally, we analyzed the river plume dynamics induced by an extreme typhoon and the influence of this event on the decrease of SSS based on comprehensive analysis of hydrometeorological datasets.

2 Methods and Materials

2.1 Study area setting

Osaka Bay, located in the eastern Seto Inland Sea of central Japan (Fig. 1), was selected as a pilot area for development of high-resolution SSS maps, because this area's distinct river plume can be expected to be induced by large runoff events from the Yodo and Yamato Rivers. The estuaries of these rivers are located in the bay head. Osaka Bay has a sloped bottom topography with a diameter of about 55 km, a mean depth of approximately 20 m, and a surface area of 1450 km^2. The bay is connected with the northwestern Pacific Ocean via the Kitan Strait and Kii Channel at the southern bay mouth and with the Harima-Nada (Harima Sea) via the Akashi Strait at the western bay mouth. Although Osaka Bay is a typical semi-enclosed bay in Japan, the subtropical, warm and saline Kuroshio water inflows intermittently into the bay through the southern bay mouth in an approximately 100-m-deep submarine valley (Yanagi, 1996). Strong tidal currents mix the riverine low-salinity water with saline water originating from the Kuroshio through the Kitan Strait (Yanagi and Takahashi, 1988a), resulting in a significant salinity gradient that increases from northeast to southwest with a salinity range of 10 to 35. Terrestrial water can remain in the bay for more than two months (Yanagi and Takahashi, 1988b). These unique oceanographic features are crucial to management of fisheries resources such as flatfishes and bivalves (e.g., Shigeta, 2008).

The annual mean discharges of the Yodo and Yamato Rivers are 268 and 19 m^3 s^{-1}, respectively, according to observed runoff data provided by the Ministry of Land, Infrastructure, Transport and Tourism of Japan (MLIT). The Yodo River drains a large catchment area (8240 km^2), which contains a population of approximately 12 million. The Yamato River (Fig. 1) has the second largest watershed (1070 km^2), but its discharge is approximately one-tenth of that from the Yodo River (Yanagi, 1980).

These two rivers provide the greatest freshwater supply to Osaka Bay, contributing up to 95% of the bay's freshwater (Hoshika et al., 1994). Other rivers flowing into the bay have small watersheds, up to approximately 496 km^2 (Muko River). The annual mean discharge from all rivers into the bay is 443 $m^3\ s^{-1}$ (Yamamoto et al., 1996).

2.2 Data Sources

2.2.1 Satellite ocean color radiometric measurements

GOCI-COMS obtains eight hourly images during the daytime and covers approximately 2,500 × 2,500 km^2 around the Japanese Islands and Korean Peninsula, centered at 36°N and 130°E with a spatial resolution of ca. 500 m and a very high signal-to-noise ratio (>1,000) (Amin et al., 2013). The expected lifespan of the GOCI mission is seven years.

GOCI has six visible bands, centered at 412, 443, 490, 555, 660, and 680 nm, and two near-infrared bands, centered at 745 nm and 865 nm. Level-1 products were downloaded from the website of the Korea Ocean Satellite Center (KOSC, http://kosc.kiost.ac/eng/p20/kosc_p21.html). We used the GOCI Data Processing System (GDPS) developed by the Korea Institute of Ocean Science and Technology (Ryu et al., 2012) to obtain well-calibrated Level-2 products converted from Level-1 data. The algorithm used to estimate a_{CDOM} in the GDPS computes the absorption coefficient of dissolved organic matter at wavelength λ=400 nm, using the remote sensing reflectance ratio of bands 1 (412 nm) to 4 (555 nm) with the equation, $a_{CDOM}(400) = 0.2355R^{-1.3423}$ m^{-1}, where, $R = R_{rs}(412)/R_{rs}(555)$ (Moon et al., 2012). Pixel data of a_{CDOM} were extracted in the study area from 34.25 to 34.75 °N and 134.85 to 135.5 °E. The acquisition period for GOCI products was from April to September in 2015 and 2016, which includes a field survey period, explained below.

2.2.2 Field survey data acquisition

Observational data were obtained by the Marine Fisheries Research Center, Research Institute of Environment, Agriculture and Fisheries, Osaka Prefectural Government (MFRC-OPG), and the Faculty of Maritime Sciences, Kobe University (FMS-KU) in four seasons from 2015 to 2016 (Table 1). MFRC-OPG makes regular observations for water temperature, salinity, and other factors collected using R/V Osaka by casting multiple water quality sensors (RINKO Profiler ASTD102; JFE Advantec Co., Ltd., Nishinomiya) at 20 fixed stations distributed throughout the bay (Fig. 1). Additionally, we conducted field observations using R/V Hakuo-Maru affiliated with FMS-KU to measure SSS by casting multiple water quality sensors (AAQ1183; JFE Advantec Co., Ltd., Nishinomiya) at 10 stations around the head of the bay. Using multiple water quality sensors, we obtained the *in situ* salinity data for surface water sampled with a bucket and sea water averaged over depths of 1–2 m observed by casting. The data were used for cross-checks.

At all observation stations, the surface water (~0.5 m) in the bay was sampled to measure the absorbance spectrum of CDOM. Here, we denote as $a_y(\lambda)$ to discriminate satellite-derived $a_{CDOM}(\lambda)$, which was used as sea truth data. The water samples obtained using a plastic bucket were stored in

glass bottles onboard the research vessels and immediately filtered through Whatman GF/F 0.45-μm glass fiber filters to remove most of the particulate matter. Each sample was filtered again through a 0.2-μm Nucleopore membrane filter to remove fine particles. The absorbance spectrum of each filtrate was scanned over the wavelength range of 300–800 nm to calculate $a_y(\lambda)$ values based on absorbance at 443 nm, $a_y(443)$ with Milli-Q water used for reference, measured by a spectrophotometer (U2900; Hitachi High-Tech Science, Tokyo) with a 10-cm-long circular quartz cylindrical cell (see Mueller et al., 2003). These observational data were used to derive the SSS–$a_y(443)$ relationship and to validate the satellite-derived absorption coefficient of CDOM, $a_{CDOM}(400)$ data after removal of error values. For validation, we compared *in situ* $a_y(443)$ with the satellite-derived $a_{CDOM}(400)$ because the *in situ* $a_y(443)$ data were highly correlated with the *in situ* $a_y(440)$ with R^2=0.99. In this study, the satellite-derived $a_{CDOM}(400)$ is referred to as a_{CDOM} for descriptive purposes.

2.2.3 Hourly *in situ* salinity data

Using the Observing System for Aquatic Quality at Automated Stations in the Osaka Bay (OSAQAS), real-time, *in situ* salinity observations have been conducted by the MLIT since April 2010. The salinity data were downloaded from the MLIT website (http://222.158.204.199/obweb/index.aspx), with an analysis period corresponding to the span of GOCI data, to allow comparison of *in situ* salinity data with satellite-derived SSS data. OSAQAS consists of observational towers and buoys at 12 stations throughout the bay (Fig. 1), and continuously collects meteorological, oceanographic, and water quality data. The water quality sensor, which travels on a rise and fall system mounted on the tower can observe salinity hourly, averaged over depths of 1–2 m. This observational layer was selected to avoid the surface salinity decrease induced by precipitation, and the layer falls within the plume because the plume bottom is at ~2 m in Osaka Bay (Fujiwara et al., 1994; Hayashi and Yanagi, 2008). Due to the potential for biofouling of in-water instrumentation, the sensors were switched out at quarterly intervals.

2.2.4 Hydrometeorological data

Precipitation data in the Yodo River watershed observations from the Automated Meteorological Data Acquisition System (AMeDAS) (Fig. 1) were obtained using the Japan Meteorological Agency website (http://www.data.jma.go.jp/gmd/risk/obsdl). Time series of daily river runoff from the Yodo River (Takahama station) were obtained from the water information system database (http://163.49.30.82) operated by the MLIT. Sites of hydrometeorological observations are shown in Fig. 1. These data were used for analysis of the relationship between river discharge (rainfall) and plumes around a typhoon. The runoff and AMeDAS data covered the analytical period.

2.3. Methodology of calibrated, satellite-derived SSS

A seven-step procedure was used to produce the satellite-derived SSS dataset calibrated by real-time *in situ* data, as follows (Fig. 2). (1) A tight *in situ* SSS–$a_y(443)$ relationship was revealed in several field

surveys, covering all seasons. (2) An accurate formula to retrieve satellite-derived a_{CDOM} was derived using *in situ* $a_y(443)$ data collected in the field surveys. (3) A robust relationship between *in situ* SSS and satellite-derived a_{CDOM} data was developed over a wide salinity range in Osaka Bay. (4) Hourly SSS was estimated from satellite-derived a_{CDOM} using the empirical relationship obtained for the *in situ* SSS and a_{CDOM}, which is called the "initial estimation". (5) Estimated SSS was compared to the hourly *in situ* SSS observed by the real-time monitoring system (OSAQAS); the difference between *in situ* and satellite-derived SSS, called offset, was obtained. (6) The offset was applied to the satellite-derived SSS map at each grid using Gaussian inter/extrapolation (Nakada and Isoda, 2000). (7) Finally, the calibrated, satellite-derived SSS (GOCI-SSS) map was produced and validated against an independent *in situ* dataset collected by the OSAQAS.

2.4 Validation of satellite-retrieved sea surface salinity

Three stations (W4, E4, and E5, Fig. 1) that were expected to represent inner-bay salinities in outer plume areas were selected for calibration of the satellite-derived SSS data. In addition, *in situ* salinity observations from two stations located at the bay head (W2 and E2) were used to validate the satellite-derived SSS, after removal of error data. To match up coincident satellite-derived and *in situ* data, satellite data acquired within 2.5 km of the stations were averaged to avoid missing data due to cloud cover directly overlying the stations. The horizontal scale of 2.5 km represents the distance that the water mass can move in approximately 1 hour with a speed 0.7 m/s, which is a typical tidal advection speed, and indicates the possible time lag of the observation timing between GOCI and *in situ* observation. We compared data from calibrated, satellite-derived SSS and contemporaneous observations of *in situ* salinity in the surface layer during the analysis period. The accuracy and precision of the satellite products were quantitatively described using the metrics of bias, root mean square error (RMSE), and determination coefficient following previous studies (e.g., Sasaki et al., 2008).

2.5 Offset maps to calibrate initial estimation of sea surface salinity

The offset maps were produced by objective analysis using Gaussian inter/extrapolation based on the difference in the hourly matchup data between the *in situ* and satellite-derived SSS, to improve the estimation accuracy of the initial estimated SSS maps. The matchup data of the satellite-derived SSS were derived at three representative observational stations (W4, E4, and E5) of OSAQAS (Fig. 1) in the same manner as for the validation. The differences derived by the matchup data were interpolated to each grid point with the same horizontal resolution of the SSS maps (500 m) in both zonal and meridional directions using a Gaussian function filter. Its e-folding horizontal scale (influence Gaussian radius) is r_G=20 km, which is nearly equal to the average distance (21.6 km) between the three stations (W4, E4, and E5). We analyzed the dependency of the number of stations and e-folding scale on the offset maps, and found that they hardly influence the offset maps, except in the period after a flood (see A1 section in Appendix).

2.6 Definition of plume boundaries

To quantify the areas and widths of river plumes, we calculated the effective boundary of the plume (Garvine, 1999), defined as the isopleth where the salinity anomaly s = 0.05. The SSS map can be converted into salinity anomaly s = $(S_a - S)/(S_a - S_i)$, where S_a(ambient salinity) and S_i (inlet salinity) represent saline water similar to open ocean water and the low-salinity water typical of an estuarine source in the bay, respectively. S_a and S_i were calculated using the area-averaged salinity over the bay region (34.3 < latitude < 34.8 and 134.9 < longitude < 135.5) and the estuarine region (34.6 < latitude < 34.8 and 135.3 < longitude < 135.5), respectively.

The inlet Rossby radius can be calculated as $r_i = \sqrt{g'\delta}/f$ (Garvine, 1999), where g' = 0.05 (m s^{-2}) is the reduced gravity, δ = 10 (m) is the water depth in the Yodo River estuary, and f is the Coriolis parameter at a latitude of 34.7° N. These parameters were used for comparison with the width of the river plumes.

3 Results

3.1. Estimation of sea surface salinity using satellite-derived a_{CDOM}

The monthly mean coverage of hourly satellite-derived a_{CDOM} data (left panel in Fig. 3a) indicates that the coverage was relatively high from 11:00 to 13:00, at up to 80%, but was generally low from 14:00 to 16:00 (up to 30%) during the analytical period. Based on eight hourly observations, the total daily coverage (right panel) always exceeded 70% except in April 2016, and was highest in August of both years. The left panel in Fig. 3b indicates that the total mean coverage for each hour was below 55% (highest at 11:00). Meanwhile, the total daily coverage (right panel) improved to nearly 80% on integration of the hourly data. There were 10 or more days per month with coverage P > 50% (Fig. 3a) in summer (July–September), but less in spring (April–June). The average number of days per month was 10.3, indicating that one-third of the data collected in a month were available for our analysis. The observational errors attributed to the solar zenith angle have less influence on our study because the data coverage at 9:00 and 16:00 was lower than 25% although the present GDPS does not remove the errors sufficiently.

As an example of a_{CDOM} observations, Fig. 4 shows a comparison between satellite-derived a_{CDOM} and *in situ* a_y(443). Most satellite-derived a_{CDOM} values were lower than 0.4 m^{-1}. The a_{CDOM} map indicates higher values in the northeastern part of the bay (approximately 0.25 m^{-1}), especially in regions along the coast of the bay head. The a_{CDOM} values decreased southwestward down to 0.05 m^{-1}. The distribution of a_y(443) is similar to that of a_{CDOM}, indicating a_y(443) data roughly covaried with a_{CDOM}. However, the a_{CDOM} values were lower than a_y(443) at two nearshore stations, which had a_y(443) values of approximately 0.4 m^{-1}, indicating substantial

underestimation of a_{CDOM}. This underestimation may be attributed to differences in observational date and time, because the fluctuation of CDOM can be greater around nearshore regions. Satellite-derived a_{CDOM} could not be obtained for the dates when field sampling was conducted (3 and 4 August) due to cloud cover. Thus, for the validation process, we used daily averaged satellite data for 5 August (5–6 h).

The scatterplot of satellite-derived a_{CDOM} and *in situ* $a_y(443)$ (Fig. 5a) using available matchup data from 5 August and 4 November shows a strong, significant correlation, with a determination coefficient of R^2=0.75 (n=60, p=3.5×10^{-19}). Regression analysis generated a good fit to the data, indicating the satellite-derived a_{CDOM} can be quantitatively verified for our analysis. Most of the corrected a_{CDOM} data (not shown) fell near the 1:1 line (RMSE: 0.034). Strong, significant correlations were also found between the observed SSS and *in situ* $a_y(443)$, with a high determination coefficient of R^2 =0.85 (n=135, p=1.5×10^{-50}) in the scatterplot (Fig. 5b) containing multiple months, indicating that seasonal dependency was minor (see section A2 in Appendix). As a result of these regression analyses, the following empirical formula was used to estimate satellite-derived SSS from satellite-derived a_{CDOM}:

$$\text{Initial estimate SSS} = -105.78\ a_{CDOM} + 44.06 \qquad (1)$$

Most estimates of SSS in the matched data followed the 1:1 line (Fig. 6), with moderate accuracy (RMSE: 1.578, bias: 0.000, R^2= 0.85, n=135, p=3.1×10^{-25}). The RMSE is sufficient to resolve the wide range of salinity (20–34) in Osaka Bay.

3.2 Accuracy of satellite-derived sea surface salinity

Figure 7 shows two examples of the initial estimated and calibrated SSS maps from 14 July and 18 August. An unrealistically low salinity distribution was visible throughout the bay on 14 July (Fig. 7a). These excessively low salinity values were successfully calibrated using hourly salinity data collected by the automatic monitoring system (OSAQAS), as shown by Fig. 7b. The SSS map on 18 August (Fig. 7c) shows high-salinity water around the Akashi Strait, which was modified by the low-salinity water distribution (Fig. 7d). These errors may be wholly or partially attributed to insufficient atmospheric correction in the GDPS algorithm or estimation errors of a_{CDOM}, as discussed in section 5. These results indicate that utilization of automated water quality monitoring data can contribute to whole or partial modification of satellite-derived SSS maps.

Next, we will show the validity of the calibrated SSS data, as verified using *in situ* SSS data derived from the OSAQAS. *In situ* SSS data were selected to match the available satellite-derived data at W4, E4, and E5 that were used for calibration (Fig. 2). The *in situ* SSS data at stations W2 and E2 in the nearshore area of the bay head were independent of the calibration data and used to validate the satellite-derived SSS. To ensure the data are sufficient for comparison, quality control was conducted on the estimated SSS data to meet the conditions of sufficient satellite data coverage over Osaka Bay

(P>15%) without extremely low or high $a_y(443)$ values, which led to the exclusion of data derived at hours 15:00 and 16:00 and on 27 April, 2 May, 29 June, and 23–28 August.

Figure 8a shows a scatterplot of the initial SSS estimates and *in situ* SSS data collected at the station, which were used for calibration. The determination coefficient was low (R^2 =0.03, n=645, p=4.3×10^{-5}) although the correlation was significant, suggesting that the accuracy of the initial estimate is insufficient for analysis (RMSE=5.1, bias=17.9). On the other hand, a strong, significant correlation (R^2 =0.57, n=645, p=2.0×10^{-120}) was found between the calibrated satellite-derived SSS and *in situ* SSS data (Fig. 8b), with data falling close to the 1:1 line (RMSE=1.5), indicating that most of the initial SSS estimates were successfully calibrated. The scatter plot of the initial estimates of SSS and *in situ* SSS data observed in the bay head (Fig. 8c) also exhibited insufficient accuracy (R^2 =0.10, n=152, p=6.9×10^{-5}, RMSE=4.6). The black dots in Fig. 8d indicate an improvement of accuracy (R^2 =0.40, n=152, p=1.3×10^{-18}) for more than half of the calibrated data (66%), which fell close to the 1:1 line (RMSE=2.9). However, the estimated SSS on 15–31 July (open circles) failed to be calibrated, because large runoff events from the Yodo River (as explained in detail below) can form low-salinity water in the nearshore area of the bay head beyond the lower limit (approximately 20) of the salinity estimation model (Fig. 6).

Thus, the accuracy of satellite-derived SSS estimation in the bay was also significantly improved by using real-time, *in situ* SSS data derived from an automated observation system (OSAQAS). As a result, the estimation error (RMSE) in the bay was decreased by 71% from the initial estimation, and the determination coefficient increased approximately 20-fold. For SSS data at stations in the nearshore area of the bay head, the estimation error (RMSE) was decreased by 37% and the determination coefficient quadrupled. The accuracy of calibrated SSS data (final estimation) is acceptable for analysis of the river plume because the plume is characterized by a wide horizontal gradient of SSS (range, 20–34).

3.3 Errors in the satellite-derived sea surface salinity

The cumulative error e_i, which the initial estimated SSS maps should retain before calibration, can be described by $e_i = \sqrt{(e_1)^2 + (e_2)^2 + (e_3)^2}$ based on the error propagation rules from procedures (1) to (4), as shown in the flowchart (Fig. 2). Here, e_1 is the error attributed to the *in situ* $a_y(443)$ estimation from the satellite-derived a_{CDOM}, e_2 is the error of the empirical formula for *in situ* SSS estimated from the *in situ* $a_y(443)$, and e_3 is the error produced by processing the initial estimation for the SSS maps. Each error can be referred to as the RMSE based on salinity; we calculated e_1=1.51 (Fig. 5a) and e_2=1.91 (Fig. 5b), but e_3 was difficult to calculate because there were multiple causes of error. Here, e_i=4.6 can be derived from the accuracy evaluation of the satellite-derived SSS (Fig. 8a). As a result, we obtained e_3=3.9 based on the error propagation rules. The contributions of each error to the cumulative error e_i^2 were also calculated as percentages, e_1^2 (10.8%), e_2^2(17.2%), and e_3^2(72.0%). The percentages indicate that the empirical formula in Eq. (1) is uniformly applied to the satellite-derived a_{CDOM} maps to be converted into the SSS in space and time, leading to the large

error contribution (72%). The calibration can significantly reduce this error (RMSE or e_c=2.9) in the case of the stations E2 and W2. Here, e_c is the error of the calibrated SSS data. These results indicate the importance of calibration using time-series of *in situ* SSS data.

4. Analysis of river plumes using SSS maps

4.1 Monthly-averaged SSS

Figure 9 shows monthly-averaged SSS maps (colors) with the effective boundaries of the plume indicated (solid lines) in Osaka Bay from August in 2015 to September 2016. The seasonal SSS patterns indicate that the river plume located in the bay head area and its salinity decreased from June to August. In this period, the plume area, demarcated by the plume boundary, shows that the plume area gradually extended southwestward from the bay head and its cross-shelf width tapered around the southwestern coast of the bay. These features are largely consistent with the findings of previous reports based on low-resolution SSS maps estimated from *in situ* observations (e.g., Nakajima, 1997), which supports the validity of the satellite-derived SSS.

The SSS maps in July (Fig. 9) show the plume distributed along the southwestern coast, suggesting that the plume flowed toward the Pacific through the eastern portion of Kitan Strait. The typical width of the low-salinity water plume was 6.9 km, comparable to the characteristic scale of the inlet Rossby radius, r_i = 7.7 km. These results suggest that the low-salinity water discharged from the river turns left along the coast and forms a growing intrusion known as a type 2 plume (Garvine, 2001). Furthermore, the small-scale patches of low-salinity water (<26) along the southwestern coast around Kansai International Airport (KIA) is visible in the satellite-derived SSS map, implying that the plume may be not only formed by runoff from the Yodo River but also from several small rivers located along the southern coast of the bay.

4.2 River plume induced by typhoon

Figure 10a shows the observed temporal variation of the daily mean Yodo River discharge and total precipitation in its watershed. The large precipitation peak on 17 July indicates heavy rainfall attributed to a Category-4 super typhoon, Nangka, leading to large discharge from the Yodo River from 17 to 18 July. Discharge gradually decreased in the post-typhoon period from 19 to 29 July, and was relatively constant at 1000 m^3 s^{-1} until 24 July, then further decreased to approximately 300 m^3 s^{-1} on July 29.

The Hovmöller diagram of SSS observations from OSAQAS (Fig. 10b) displayed temporal variation of low-salinity surface water in response to large runoff events. SSS observed in the pre-typhoon period exhibited low salinity 14–26 around the estuary (W2, W1, E1, and E2) and increased to 30 during the typhoon at E1, implying that vertical mixing was enhanced by the strong wind. Then, the salinity decreased due to the large freshwater input on 17 July; low-salinity water

appeared again on 18 July, which rapidly extended westward and southward to the Akashi and Kitan Straits along the west and east coasts, respectively.

The SSS distributions differ notably between the pre- and post-typhoon periods (Fig. 11). Comparing the distributions on 15 and 20 July indicated that low-salinity water in the bay head spread southward after the large runoff peak on 18 July, and extended along the southeast coast around KIA. The eastern front of low salinity water intruded into Akashi Strait. Based on the effective boundary of the plume in the bay head, the area within the plume changed from 360.1 km^2 in the pre-typhoon period to 533.1 km^2 post-typhoon. The post-typhoon plume covered half of Osaka Bay; the change in area associated with the runoff peak was approximately 1.5-fold. Hourly changes in low salinity water were rarely found, suggesting that estimation errors in the areas attributed to wind-driven or tidal transport of the low-salinity water were negligible in this period.

Figure 12a shows the temporal change in the area within the daily-averaged effective boundary of the plume. This figure indicates that low-salinity water migrated southwestward to the bay mouth in the post-typhoon period. The migration speed was approximately 7 km day^{-1} (0.08 m s^{-1}). A jut in the boundary was visible in the center of the bay on 25 July, and this jut propagated southwestward along the bay axis, leading to an extension of the low-salinity water in the southern part of the bay. Then, the low-salinity water flowed out through Kitan Strait in the period of 26 to 29 July, while a large area of low-salinity water (<26) remained in the eastern portion of the bay on 29 July (Fig. 12b). The area of low-salinity water shrank nearly to its pre-typhoon extent on 31 July, indicating that the duration of the SSS decrease in the bay induced by the large freshwater discharge from the typhoon was approximately two weeks.

5. Discussion

This paper presents a methodology to produce and improve high-resolution SSS maps in ROFI based on ocean color observations from a geostationary satellite in conjunction with an automated observing system (OSAQAS) to collect time-series *in situ* SSS data. The implementation of a procedure to calibrate SSS could suppress two types of estimation errors. One of these is error in the empirical formula for the SSS–a_{CDOM} relationship, which can be attributed to regional hydrodynamic and biogeochemical processes (Bai et al., 2013). In local coastal waters, an empirical methodology based on the SSS–a_{CDOM} relationship may be regulated by regional and seasonal variations (Bai et al., 2013). For example, marine CDOM sources (autochthonous production of CDOM) can be induced by sediment resuspension associated with atmospheric disturbances (Boss et al., 2001) and by biological effects such as the degradation of coastal phytoplankton and microbial decomposition (Nelson et al., 1998, 2010; Twardowski and Donaghay, 2001; Coble et al., 2004; Stedmon and Markager). On the other hand, decreases in CDOM can be induced by microbial consumption (Del Vecchio and Blough, 2004) and photochemical bleaching (Chen et al., 2004) of labile and semi-labile DOM (Keller and Hood, 2011; Kobayashi et al., 2017). Errors attributable to these processes may affect the SSS map on

18 August (Fig. 7), in which a lower SSS range around the estuary and bay head was estimated before local calibration. However, seasonal and regional variations in the SSS–$a_y(443)$ relationship in Osaka Bay were rarely observed in the field surveys. Another estimation error can be attributed to the atmospheric correction algorithm used for remote sensing reflectance (e.g., He et al., 2012; Wang et al., 2007) and the bio-optical model used to estimate a_{CDOM} (e.g., Lee et al., 2002; Zhu et al., 2011). Errors attributed to these complex processes can propagate and limit the accuracy of satellite-derived a_{CDOM}, leading to unrealistically low SSS, as was seen on 14 July (Fig. 7). This result implies that the increase of land-based aerosols may not be fully accounted for in the atmospheric correction algorithm (Vogel and Brown, 2016), leading to overestimation of a_{CDOM} in the bay.

Our results suggest that the observations of SSS time-series at appropriate locations in the coastal sea is essential for practical application of satellite-derived SSS to the coastal sea, although efforts should be undertaken in the future to improve the satellite-derived a_{CDOM} algorithm in coastal waters. In Japanese coastal seas, automated systems to observe salinity, such as OSAQAS, are already operating in larger bays (e.g., Ise Bay, Tokyo Bay, and Funka Bay), showing that our approach can be applied immediately in those coastal areas. Note that the application of our methodology to other coastal seas is possible under the following three assumptions: 1) the spatiotemporal variation in the SSS is mainly dominated by freshwater supply via the riverine discharge and its mixing with coastal seawater, 2) the terrestrial CDOM in the coastal seas greatly exceed the marine CDOM, and 3) the horizontal pattern in satellite-derived a_{CDOM} maps may be qualitative because the GOCI observations could retain an unknown large-scale bias.

Typhoons (tropical storms) are the most energetic extreme weather events affecting the environment and ecosystem in estuarine and coastal areas (Herbeck et al., 2011). However, the dynamics of river plumes formed by large runoff events caused by typhoon strikes remain poorly understood. These events have been studied primarily using numerical modeling (e.g., Liu et al., 2002) due to the absence of observations collected at high temporal frequency and horizontal density. Our results show the detailed dynamics of the river plume influenced by extreme runoff during the typhoon period in Osaka Bay. The low-salinity water of the plume tends to be distributed from Kobe City to Akashi Strait along the northern coast (Fig. 11), supporting the westward advection of the plume when discharge from the Yodo River increases markedly due to flood events (Fujiwara et al., 1994a). Then, the plume migrated southwestward along the east coast toward the bay mouth (Fig. 12), with a migration speed of 0.08 m/s, comparable to the flow speed of the Okino-se circulation (Fujiwara et al., 1994b) but smaller than the propagation speed of an internal Kelvin wave, $Ci = \sqrt{g'\delta} = 0.7$ m s^{-1}. Therefore, the Okino-se circulation may play an important role in transporting the river plume, high in nutrients and turbidity, to outer Osaka Bay through the Kitan Strait within two weeks after a typhoon. Thus, SSS data with high spatiotemporal resolution can be used to observe the marked increase in low-salinity water induced by typhoons. Additional studies may provide further statistical analysis of the detailed plume dynamics when satellite-derived SSS data surrounding typhoon events are accumulated in the future.

6. Conclusions

This paper proposed a novel methodology to produce spatiotemporally high-resolution (~500 m) SSS maps for analysis of the river plume and coastal oceans at a local scale (~10^3 km^3), based on hourly ocean color products derived from geostationary satellite observations. The estimation accuracy of the satellite-derived SSS data was improved by utilization of time-series *in situ* SSS data collected by an automated observation system. As a result, estimation error of satellite-derived SSS substantially decreased (37 to 71%) within a wide range of SSS (20–34). Dynamics of the river plume induced by typhoon-generated runoff was first comprehensively investigated using time-series *in situ* SSS and hydrological data and a satellite-derived SSS (GOCI-SSS) map. After calculating the salinity anomaly based on the satellite-derived SSS map, the effective boundary of the plume could be used to identify quantitatively the area and width of river plumes. The plume area covered half of the bay during the post-typhoon period, and was approximately 1.5 times as large as in the pre-typhoon period, leading to a decrease of the SSS in the bay during the two weeks following the storm. The plume in the bay head intruded into the Akashi Strait after the large runoff event, while the plume also extended southward along the southeast coast to the bay mouth, where it flowed out through Kitan Strait. Our approach provides a practical method of analyzing the dynamics of low-salinity riverine plumes in coastal oceans, which may lead to the development of improved coastal ocean models for operational oceanography, ocean forecasting (Urakawa et al., 2016), and disaster reduction (Nakada et al., 2016).

Acknowledgements

This work was supported primarily by the Fund of the Japan Society for the Promotion of Science (No. 26887025, No. 16K13882) and the Kurita Water and Environment Foundation (KWEF), Japan, and was carried out in part by the Collaborative Research Program of Research Institute for Applied Mechanics, Kyushu University and the joint research program of the Institute for Space-Earth Environmental Research (ISEE), Nagoya University. The authors sincerely thank Dr. T. Yanagi in the EMECS center and Prof. M. Hayashi at Kobe University for their comments. Part of this work used the computational resources of the supercomputer ACCMS, Kyoto University. We deeply appreciate the constructive comments from two anonymous reviewers and editor, Prof. T. Hirawake.

REFERENCES

Amin R, Gould R, Ladner S, Shulman I, Jolliff J, Sakalaukus P, Lawson A, Martinolich P, Arnone R (2013) Inter-Sensor Comparison of Satellite Ocean Color Products from GOCI and MODIS. AMS Proceedings, pp5.

Bai Y, Pan D, Cai W, He X, Wang D, Tao B, Zhu Q (2013) Remote sensing of salinity from satellite-derived CDOM in the Changjiang River dominated East China Sea. Journal of Geophysical Research: Oceans 118:227-243 doi:10.1029/2012JC008467

Bai Y, He X, Pan D, Chen CTA, Kang Y, Chen X, Cai WJ (2014) Summertime Changjiang River plume variation during 1998–2010. Journal of Geophysical Research: Oceans, 119:6238–6257. doi:10.1002/2014JC009866.

Binding CE, Bowers DG (2003) Measuring the salinity of the Clyde Sea from remotely sensed ocean colour. Estuarine, Coastal and Shelf Science 57:605–611. doi:10.1016/S0272-7714(02)00399-2

Bowers DG, Brett HL (2008) The relationship between CDOM and salinity in estuaries: an analytical and graphical solution. Journal of Marine Systems 73(1–2):1–7

Boss E, Pegau WS, Zaneveld JRV, Barnard AH (2001) Spatial and temporal variability of absorption by dissolved material at a continental shelf. Journal of Geophysical Research, 106:9499–9507.

Chen Z, Li Y, Pan J (2004) Distributions of colored dissolved organic matter and dissolved organic carbon in the Pearl River Estuary, China. Continental Shelf Research 24:1845–1856.

Coble P, Hu C, Gould Jr RW, Chang G, Wood AM (2004) Colored Dissolved Organic Matter in the Coastal Ocean: An Optical Tool for Coastal Zone Environmental assessment and management, Oceanography, 17(2):50–59.

Del Castillo CE, Coble PG, Morell JM, Lopez JM, Corredor JE (1999) Analysis of the optical properties of the Orinoco River plume by absorption and fluorescence spectroscopy. Marine Chemistry 66(1–2):35–51

Del Castillo CE, Miller RL (2008) On the use of ocean color remote sensing to measure the transport of dissolved organic carbon by the Mississippi River Plume. Remote Sensing of Environment, 112:836–844. doi:10.1016/j.rse.2007.06.015

Del Vecchio R, Subramaniam A (2004) Influence of the Amazon River on the surface optical properties of the western tropical North Atlantic Ocean. Journal of Geophysical Research, 109:C11001. doi:10.1029/2004JC002503

Fichot CG, Lohrenz SE, Benner R (2014) Pulsed, cross-shelf export of terrigenous dissolved organic carbon to the Gulf of Mexico. Journal of Geophysical Research: Oceans 119(2):1176–1194 doi: 10.1002/2013JC009424

Font J, Camps A, Borges A, Martín-Neira M, Boutin J, Reul N, Kerr YH, Hahne A, Mecklenburg S (2010) SMOS: The challenging sea surface salinity measurement from space. Proc. IEEE, 98(5):649–665 doi:10.1109/JPROC.2009.2033096

Fujiwara T, Sawada Y, Nakatsuji K, Kuramoto S (1994a) Water exchange time and flow characteristics

of the upper water in the eastern Osaka Bay –Anticyclonic circulation in the head of the estuary. Bull. Coastal Oceanography, 31(2):227–238 (in Japanese with English abstract).

Fujiwara T, Nakata H, Nakatsuji K (1994b) Tidal-jet and vortex-pair driving of the residual circulation in a tidal estuary. Continental Shelf Research, 14(9):1025–1038.

Garvine RW (1999) Penetration of buoyant coastal discharge onto the continental shelf: A numerical model experiment. Journal of Physical Oceanography 29:1892–1909

Garvine RW (2001) The impact of model con guration in studies of buoyant coastal discharge. Journal of Marine Research, 59:193–225.

Geiger EF, Grossi MD, Trembanis AC, Kohut JT, Oliver MJ (2013) Satellite-derived coastal ocean and estuarine salinity in the Mid- Atlantic. Continental Shelf Research 63:S235–S242. doi:10.1016/j.csr.2011.12.001

Hayashi M, Yanagi T (2008) Analysis of change of red tide species in Yodo River estuary by the numerical ecosystem model. Marine Pollution Bulletin, 57:103–107. doi:10.1016/j.marpolbul.2008.04.015

Hansell DA (2013) Recalcitrant dissolved organic carbon fractions. Annual Review of Marine Science, 5:421–445. doi:10.1146/annurev-marine-120710-100757

He X, Bai Y, Pan D, Tang J, Wang D (2012) Atmospheric correction of satellite ocean color imagery using the ultraviolet wavelength for highly turbid waters. OPTICS EXPRESS, 20(18):20754–20770.

Herbeck LS, Unger D, Krummea U, Liu SM, Jennerjahn TC (2011) Typhoon-induced precipitation impact on nutrient and suspended matter dynamics of a tropical estuary affected by human activities in Hainan, China. Estuarine, Coastal and Shelf Science 93:375–388

Hoshika A, Tanimoto T, Mishima Y (1994) Sedimentation Processes of Particulate Matter in the Osaka Bay. Oceanography in Japan, 3(6): 419–425.

Hu C, Montgomery ET, Schmitt RW, Muller-Karger FE (2004) The dispersal of the Amazon and Orinoco River water in the tropical Atlantic and Caribbean Sea: Observation from space and S-PALACE floats. Deep-Sea Research II, 51:1151–1171. doi:10.1016/j.dsr2.2004.04.001

Kawahara M, Uye S, Ohtsu K, Iizumi H (2006) Unusual population explosion of the giant jellyfish *Nemopilema nomurai* (Scyphozoa: Rhizostomeae) in East Asian waters. Marine Ecology Progress Series 307:161-173

Kerr YH, Waldteufel P, Wigneron J, Delwart S, Cabot F, Boutin J, Escorihuela MJ, Font J, Reul N, Gruhier C (2010) The SMOS mission: Newtool for monitoring key elements of the global water cycle. Proc. IEEE, 98(5):666–687 doi:10.1109/JPROC.2010.2043032

Keller DP, Hood RR (2011) Modeling the seasonal autochthonous sources of dissolved organic carbon and nitrogen in the upper Chesapeake Bay. Ecological Modelling 222:1139–1162

Kobayashi S, Matsumura Y, Kawamura K, Nakajima M, Yamamoto K, Akiyama S, Ueta Y (2017) Estimation of the Origin of Dissolved Organic Matter and Biogeochemical Cycles of Nutrients in Osaka Bay, Japan. Journal of Japan Society on Water Environment 40(2):1–9.

Kuroda H, Takahashi D, Mitsudera H, Azumaya T, Setou T (2014) A preliminary study to understand the transport process for the eggs and larvae of Japanese Pacific walleye Pollock *Theragra chalcogramma* using particle-tracking experiments based on a high-resolution ocean model. Fisheries Science. DOI 10.1007/s12562-014-0717-y

Kusaka A, Tomonori Azumaya T, Kawasaki Y (2013) Monthly variations of hydrographic structures and water mass distribution off the Doto area, Japan. Journal of Oceanography, 69:295–312. DOI 10.1007/s10872-013-0174-8

Koblinsky CJ, Hildebrand P, LeVine D, Pellerano F, Chao Y, Wilson W, Yueh S, Lagerloef G (2003) Sea surface salinity from space: Science goals and measurement approach. Radio Sci. 38(4):8064 doi:10.1029/2001RS002584

Lagerloef GSE, Colomb F, LeVine DM, Wentz F, Yueh S, Ruf C, Lilly J, Gunn J, Chao Y, de Charon A, Feldman G, Swift C (2008) The Aquarius/SAC-D mission: designed to meet the salinity remote-sensing challenge. Oceanography, 21(1), 68–81.

Lee ZP, Carder KL, Arnone RA (2002) Deriving inherent optical properties from water color: a multiband quasi-analytical algorithm for optically deep waters. APPLIED OPTICS, 41(27):5755–5772.

Liu JT, Chao S, Hsu RT (2002) Numerical modeling study of sediment dispersal by a river plume. Continental Shelf Research, 22:1745–1773.

Mueller JL, Fargion GS, McClain CR, Pegau S, Mitchell BG, Kahru M, Wieland J, Stramska M (2003) Inherent optical properties: Instruments, characterizations, field measurements and data analysis protocols. NASA Tech. Memo., NASA/TM-2003–211621/4(4).

Molleri GSF, Novo EMLM, Kampel M (2010) Space-time variability of the Amazon River plume based on satellite ocean color. Continental Shelf Research, 30:342–352. doi:10.1016/j.csr.2009.11.015

Moon JE, Park YJ, Ryu JH, Choi JK, Ahn JH, Min JE, Son YB, Lee SJ, Han HJ, Ahn YH (2012) Initial validation of GOCI water products against in situ data collected around Korean peninsula for 2010–2011, Ocean Science Journal, 47:261–277. doi:10.1007/s12601-012-0027-1

Nakajima M (1997) Structure of Stratification and Changes in Water Quality of Osaka Bay. Umi to Sora, 73(1):15-21 (in Japanese with English abstract)

Nakada S, Isoda Y (2000) Seasonal variation of the Tsusima Warm Current off Toyama Bay. Umi to Sora 76:17–24 (in Japanese with English abstract)

Nakada S, Ishikawa Y, Awaji T, In T, Shima S, Nakayama T, Isada T, Saitoh S (2012), Modeling Runoff into a Region Of Freshwater Influence for Improved Ocean Prediction: An Application in Funka Bay, Hydrological Research Letters, 6, 47–52.

Nakada S, Baba K, Sato M, Natsuike M, Ishikawa Y, Awaji T, Koyamada K, Saitoh SI (2014) The role of snowmelt runoff on the ocean environment and scallop production in Funka Bay, Japan. Progress in Earth and Planetary Science 1:25 DOI: 10.3178/HRL.6.47

Nakada S, Hayashi M, Koshimura S, Yoneda S, Kobayashi E (2016): Tsunami-Tide Simulation in a

Large Bay Based on the Greatest Earthquake Scenario Along the Nankai Trough, International Journal of Offshore and Polar Engineering, 26(4), 392-400.

Nakada S, Hayashi M, Koshimura S, Taniguchi Y, Kobayashi E, (2017) Salinization by Tsunami in a semi-enclosed bay: Tsunami-Ocean 3D simulation based on the great earthquake scenario along the Nankai Trough, J. Adv. Simulat. Sci. Eng., 3(2):206–214.

Nelson NB, Siegel DA, Michaels AF (1998) Seasonal dynamics of colored dissolved material in the Sargasso Sea. Deep-Sea Research I 45:931–957

Nelson NB, Siegel DA, Carlson CA, Swan CM (2010) Tracing global biogeochemical cycles and meridional overturning circulation using chromophoric dissolved organic matter. Geophysical Research Letters, 37:L03610. doi:10.1029/2009GL042325

Qing S, Zhang J, Cui T, Bao Y (2013) Retrieval of sea surface salinity with MERIS and MODIS data in the Bohai Sea. Remote Sensing of Environment, 136:117–125. doi.org/10.1016/j.rse.2013.04.016

Ryu JH, Han HJ, Cho S, Park YJ, Ahn YH (2012) Overview of Geostationary Ocean Color Imager (GOCI) and GOCI Data Processing System (GDPS). Ocean Science Journal, 47(3):223–233. http://dx.doi.org/10.1007/s12601-012-0024-4

Sakamoto K, Yamanaka G, Tsujino H, Nakano H, Urakawa S, Usui N, Hirabara M, Ogawa K (2016) Development of an operational coastal model of the Seto Inland Sea, Japan. Journal of Oceanography, 66:77–97. DOI 10.1007/s10236-015-0908-9

Sasaki H, Siswanto E, Nishiuchi K, Tanaka K, Hasegawa T, Ishizaka J (2008) Mapping the low salinity Changjiang Diluted Water using satellite-retrieved colored dissolved organic matter (CDOM) in the East China Sea during high river flow season. Geophysical Research Letters 35:L04604 doi:10.1029/2007GL032637

Senjyu T, Okuno J, Ookei N, Tsuji T (2013) Behavior of surface low salinity water and mass occurrence of giant jellyfish (*Nemopilema nomurai*) in the coastal area of the Japan Sea in summer 2009. Umi to Sora 89(2):53–60 (in Japanese with English abstract)

Shigeta T (2008) Recent ecological problems of the fishes in the Seto Inland Sea, Japan. Nippon Suisan Gakkaishi, 74(5):868–872.

Simpson JH (1997) Physical processes in the ROFI regime. Journal of Marine Systems, 12:3–15

Son YB, Gardner WD, Richardson MJ, Ishizaka J, Ryu JH, Kim SH, Lee SH (2012) Tracing offshore low-salinity plumes in the Northeastern Gulf of Mexico during the summer season by use of multispectral remote-sensing data. Journal of Oceanography, 71:1–19. DOI 10.1007/s10872-012-0131-y

Stedmon CA, Markager S (2005) Tracing the production and degradation of autochthonous fractions of dissolved organic matter by fluorescence analysis. Limnology and Oceanography, 50(5):1415–1426.

Takagi S, Nanba Y, Fujisawa T, Watanabe Y, Fujiwara T (2012) River-water spread in Bisan Strait with reference to nutrient supply to nori (*Porphyra*) farms. Bull Jpn Soc Fish Oceanogr 76(4):197–204 (in Japanese with English abstract)

Twardowski MS, Donaghay PL (2001) Separating in situ and terrigenous sources of absorption by dissolved materials in coastal waters. Journal of Geophysical Research, 106:2545–2560

Urquhart EA, Zaitchik BF, Hoffman MJ, Guikema SD, Geiger EF (2012) Remotely sensed estimates of surface salinity in the Chesapeake Bay: a statistical approach. Remote Sensing of Environment, 123:522–531. doi:10.1016/j.rse.2012.04.008

Urakawa LS, Kurogi M, Yoshimura K, Hasumi H (2015) Modeling low salinity waters along the coast around Japan using a high‐resolution river discharge dataset. Journal of Oceanography, 71:715–739. DOI 10.1007/s10872-015-0314-4

Del Vecchio R, Neil V. Blough (2004) Spatial and seasonal distribution of chromophoric dissolved organic matter and dissolved organic carbon in the Middle Atlantic Bight. Marine Chemistry 89:169–187.

Vogel RL, Brown CW (2016) Assessing satellite sea surface salinity from ocean color radiometric measurements for coastal hydrodynamic model data assimilation. Journal of Applied Remote Sensing 10(3):036003 doi: 10.1117/1.JRS.10.036003.

Wang M, Tang J, Shi W (2007) MODIS-derived ocean color products along the China east coastal region. Geophysical Research Letters, 34:L06611. doi:10.1029/2006GL028599

Wouthuyzen S, Tarigan S, Kusmanto E, Supriyadi HI, Sediadi A, Sugarin, Siregar VP, Ishizaka J (2011) Measuring sea surface salinity of the jakarta bay using remotely sensed of ocean color data acquired by modis sensor. Mar. Res. Indonesia, 36(2):51−70.

Yamamoto T, Kitamura T, Matsuda O (1996) Riverine inputs of fresh water, total nitrogen and total phosphorus into the Seto Inland Sea. J. Fac. Appl. Biol. Sci., Hiroshima Univ., 35:81−104.

Yanagi T (1980) Variability of the constant flow in Osaka Bay. Journal of the Oceanography Society of Japan, 36252.

Yanagi T (1996) Effects of open ocean variability to the oceanic condition of Osaka Bay and Kii Channel. Bull. Coastal Oceanography, 34(1):53–57 (in Japanese with English abstract).

Yanagi T, Takahashi S (1988a) A tidal front influenced by river discharge. Dynamics of Atmospheres and Oceans, 12:191−206.

Yanagi T, Takahashi S (1988b) Response to fresh water discharge in Osaka Bay. Umi to Sola, 64(2):1−8 (in Japanese with English abstract).

Zhu W, Yu Q, Tian YQ, Chen RF, Gardner GB (2011) Estimation of chromophoric dissolved organic matter in the Mississippi and Atchafalaya river plume regions using above‐surface hyperspectral remote sensing. Journal of Geophysical Research, 116:C02011. doi:10.1029/2010JC006523

Figure captions

Fig. 1 (a) Map of the study area showing watersheds and river paths flowing into Osaka Bay, which is located in the central region of the main island of Japan, indicated by the red-shaded square in the upper-left map. The color scale in the bay indicates depth in meters. Blue and green colors on land indicate the watersheds of the Yodo River and Yamato River, respectively. Red squares denote the area analyzed with satellite ocean color data. White dots represent Automated Meteorological Data Acquisition System (AMeDAS) stations, and the red dot represents the river observation station at Takahama. (b) Map of *in situ* observational stations and water sampling sites for $a_y(443)$. The green dots indicate stations regularly monitored by the Marine Fisheries Research Center, Research Institute of Environment, Agriculture and Fisheries, Osaka Prefectural Government (MFRC-OPG). Black circles indicate stations occasionally sampled by the Faculty of Maritime Sciences, Kobe University (FMSKU). Rectangles indicate stations of the Observing System for Aquatic Quality at Automated Stations in the Osaka Bay (OSAQAS). The data collected at the stations denoted by the red and blue rectangles were used for calibration and validation of the satellite-derived SSS map, respectively. The data collected at stations marked by black rectangles were not used. Blue arrows indicate river flow inlets.

Fig. 2 Flowchart for obtaining initial estimates and calibrated sea surface salinity values from the combined dataset of ocean color satellite, automated observing system (OSAQAS), and hydrographic observations. Numbers indicate the process sequence as explained in section 2.3.

Fig. 3 (a) Monthly mean coverages over the analytic area in each hour of ocean color satellite observation during the analytic period from April to September of 2015 and 2016 (left panel). The right panel shows monthly mean values of total daily coverage and total days per month with coverage of more than half of the analytic area (P > 50%). (b) Coverage averaged over the analytic period in hourly (left), and average days with P > 50% (right).

Fig. 4 Geographic distribution of satellite-derived a_{CDOM} and *in situ* (observed) $a_y(443)$ (m^{-1}) on 5 August and 3–4 August, 2015, respectively.

Fig. 5 (a) Scatter plot comparing satellite-derived a_{CDOM} and *in situ* (observed) $a_y(443)$ (m^{-1}) data in match-up periods from 3–5 August and 2–4 November 2015. (b) Scatter plot showing *in situ* $a_y(443)$ (m^{-1}) and *in situ* sea surface salinity in summer (August 2015), fall (October, and November 2015), winter (February 2016) and spring (May 2016). Gray lines represent the 95% prediction interval.

Fig. 6 Comparison of satellite-derived and observed (*in situ*) sea surface salinity. Gray lines and areas represent the 95% prediction interval.

Fig. 7 Maps of satellite-derived sea surface salinity from the initial estimate before calibration (a and c) and final estimate after calibration (b and d) on 14 July and 18 August, 2015.

Fig. 8 Comparison of initial estimates (left panels) and calibrated values (right panels) of sea surface salinity. *In situ* salinity, used in the upper and lower panels, was observed at the western offshore stations (W4, E4, and E5: red rectangles in Fig. 1) of OSAQAS and at the stations in the bay head (W2 and E2: blue rectangles), respectively. Plots were divided into a group with RMSE < 1.5 (black dots) and other data (open gray circles).

Fig. 9 Maps of monthly mean, sea surface salinity collected by GOCI-COMS from April to September of the analysis period. Solid lines indicate the effective boundary of the plume. Pale blue lines in the watershed indicate river paths.

Fig. 10 (a) Temporal variations in total daily precipitation ($m^3\ s^{-1}$) estimated from AMeDAS data over the Yodo River watershed and runoff ($m^3\ s^{-1}$) observed at Takahama (Fig. 1) during the pre-typhoon to post-typhoon period (10–29 July 2015). Solid lines indicate days for which satellite data were available. (b) Hovmöller diagrams of hourly nearshore sea surface salinity along the coast of the bay from 10–29 July 2015. The ten letter and number combinations (E1-E5 and W1-W5) correspond to the OSAQAS stations (Fig. 1). Stations E1 and W1, as shown on the vertical axis, are located in the estuaries of the Yodo and Yamato Rivers, respectively. Black rectangles in the diagram indicate missing data.

Fig. 11 Hourly maps of sea surface salinity derived from GOCI-COMS in the pre-typhoon (15 July 2015) and post-typhoon (20 July 2015) periods. Solid lines indicate the effective boundary of the plume.

Fig. 12 (a) Temporal variation of the effective boundary of the plume from 15 to 26 July 2015. (b) Map of sea surface salinity and the effective boundary of the plume (solid line) on 29 July 2015.

Table 1 Dates of observations conducted aboard the R/V Osaka (Marine Fisheries Research Center, Research Institute of Environment, Agriculture and Fisheries, Osaka Prefectural Government; MFRC-OPG) and the R/V Hakuo-Maru (Faculty of Maritime Sciences, Kobe University; FMS-KU).

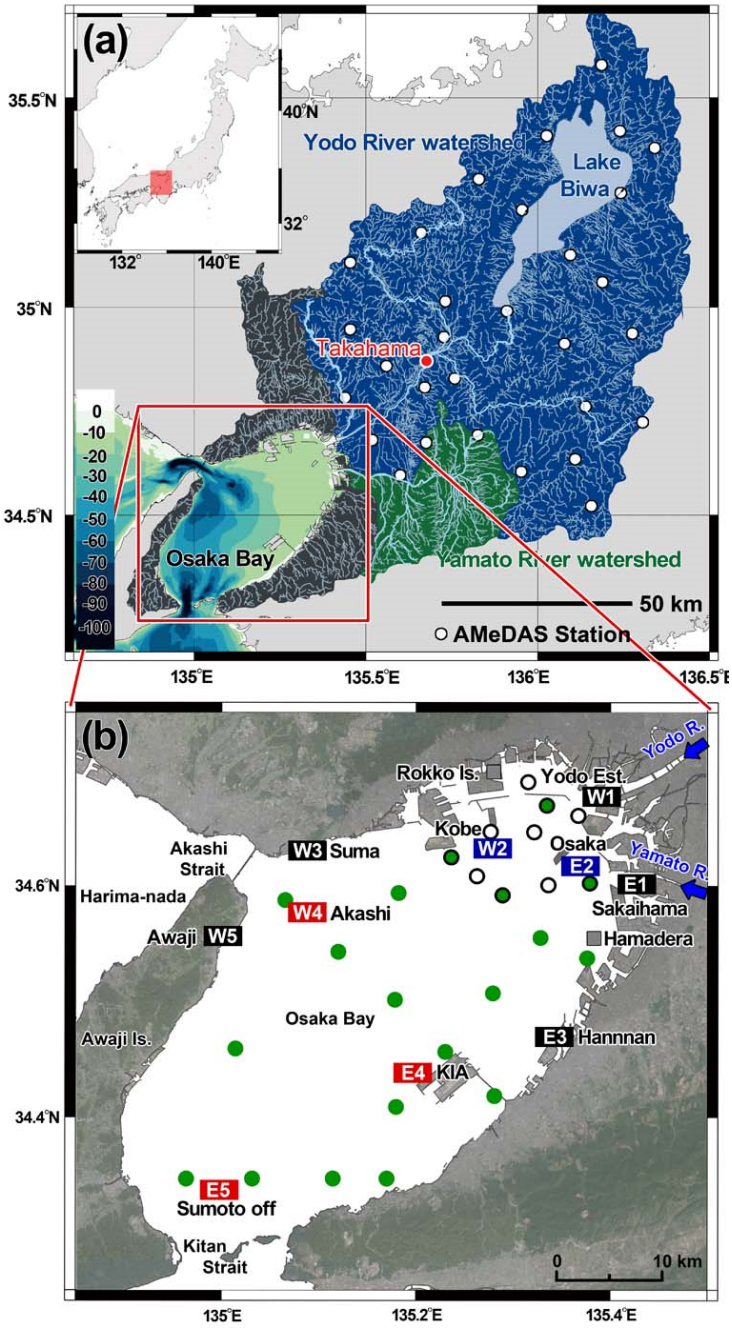

Figure 1 (a) Map of the study area showing watersheds and river paths flowing into Osaka Bay, which is located in the central region of the main island of Japan, indicated by the red-shaded square in the upper-left map. The color scale in the bay indicates depth in meters. Blue and green colors on land indicate the watersheds of the Yodo River and Yamato River, respectively. Red squares denote the area analyzed with satellite ocean color data. White dots represent Automated Meteorological Data Acquisition System (AMeDAS) stations, and the red dot represents the river observation station at Takahama. (b) Map of *in situ* observational stations and water sampling sites for $a_y(443)$. The green dots indicate stations regularly monitored by the Marine Fisheries Research Center, Research Institute of Environment, Agriculture and Fisheries, Osaka Prefectural Government (MFRC-OPG). Black circles indicate stations occasionally sampled by the Faculty of Maritime Sciences, Kobe University (FMSKU). Rectangles indicate stations of the Observing System for Aquatic Quality at Automated Stations in the Osaka Bay (OSAQAS). The data collected at the stations denoted by the red and blue rectangles were used for calibration and validation of the satellite-derived SSS map, respectively. The data collected at stations marked by black rectangles were not used. Blue arrows indicate river flow inlets.

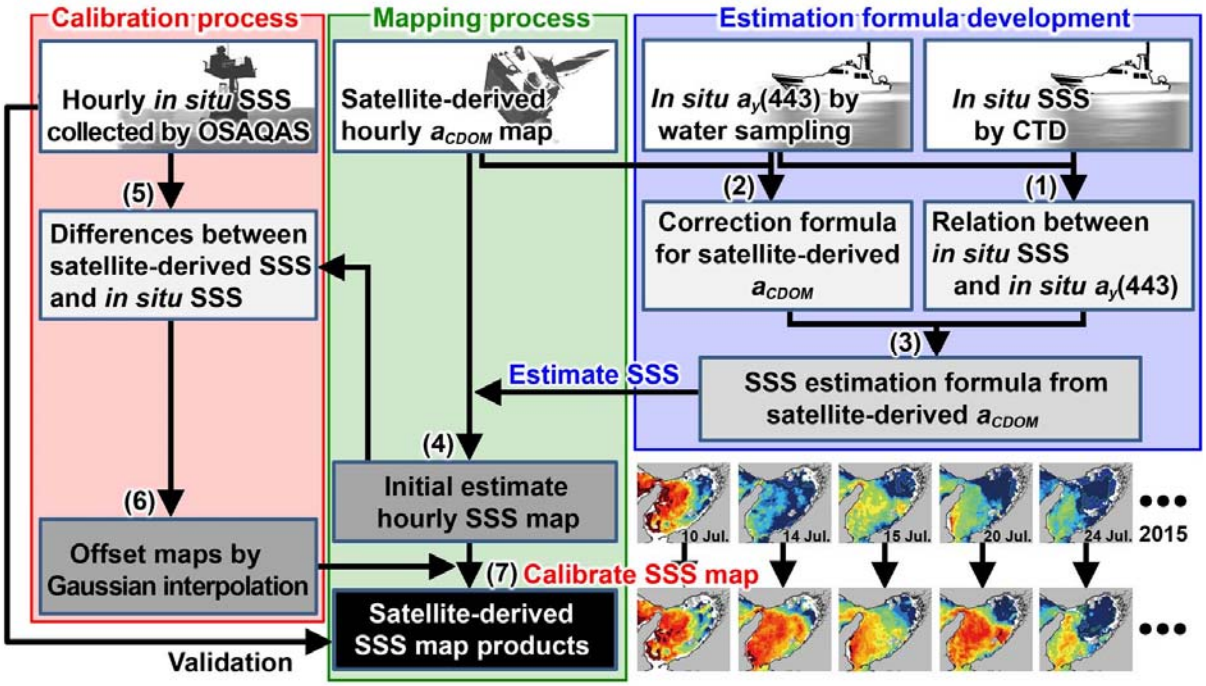

Figure 2 Flowchart for obtaining initial estimates and calibrated sea surface salinity values from the combined dataset of ocean color satellite, automated observing system (OSAQAS), and hydrographic observations. Numbers indicate the process sequence as explained in section 2.3.

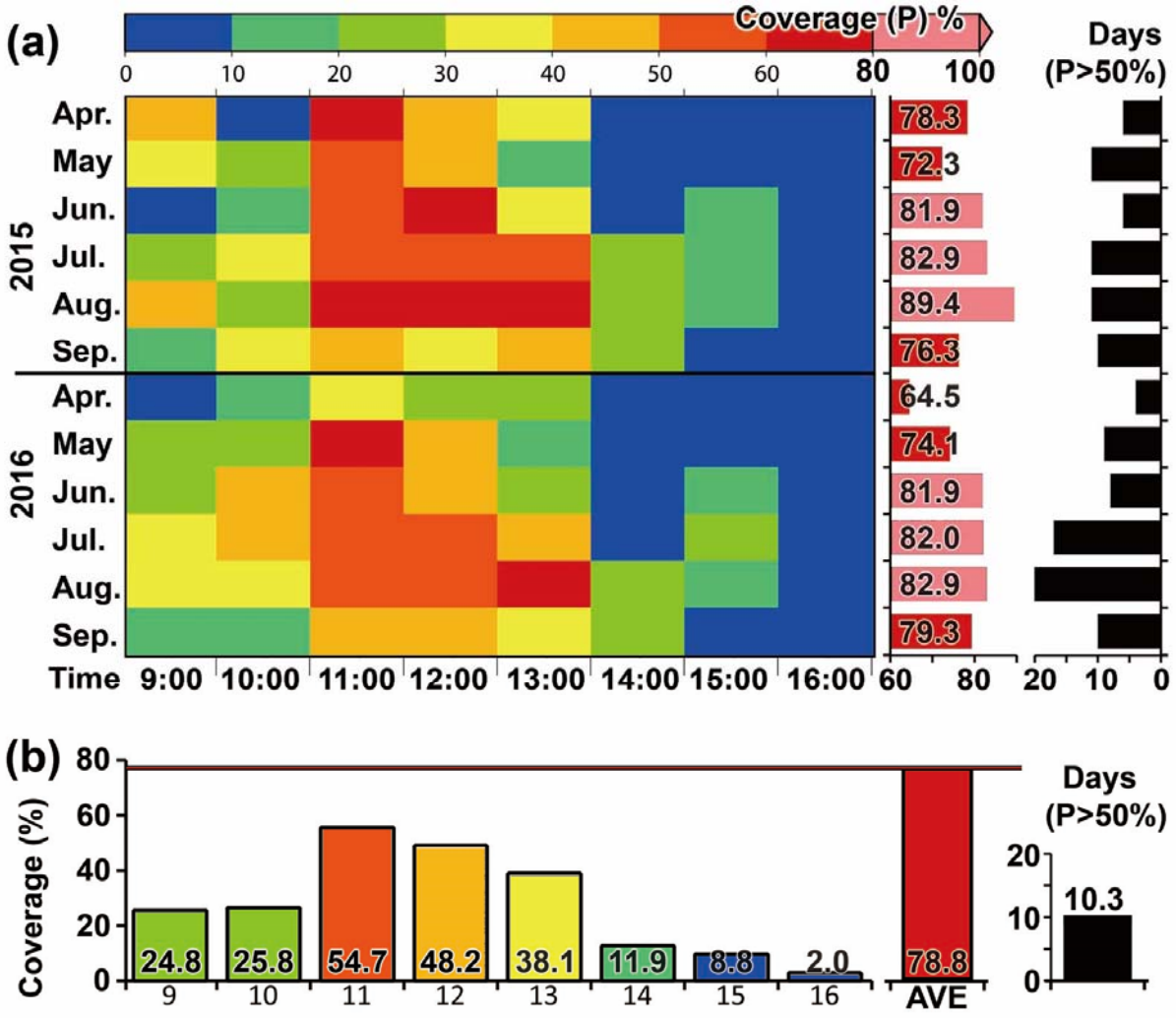

Figure 3 (a) Monthly mean coverages over the analytic area in each hour of ocean color satellite observation during the analytic period from April to September of 2015 and 2016 (left panel). The right panel shows monthly mean values of total daily coverage and total days per month with coverage of more than half of the analytic area (P > 50%). (b) Coverage averaged over the analytic period in hourly (left), and average days with P > 50% (right).

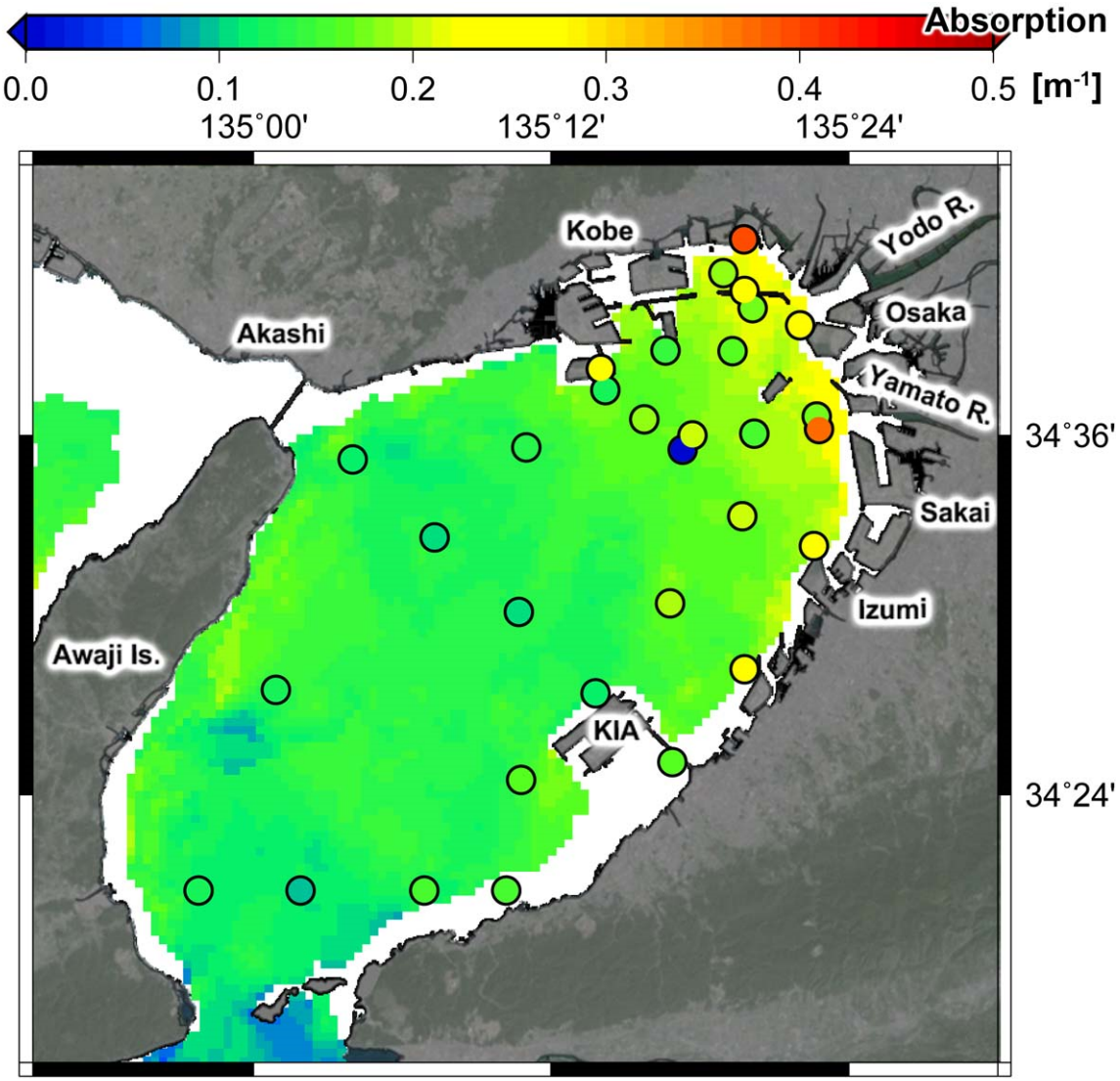

Figure 4 Geographic distribution of satellite-derived a_{CDOM} and *in situ* (observed) $a_y(443)$ (m^{-1}) on 5 August and 3–4 August, 2015, respectively.

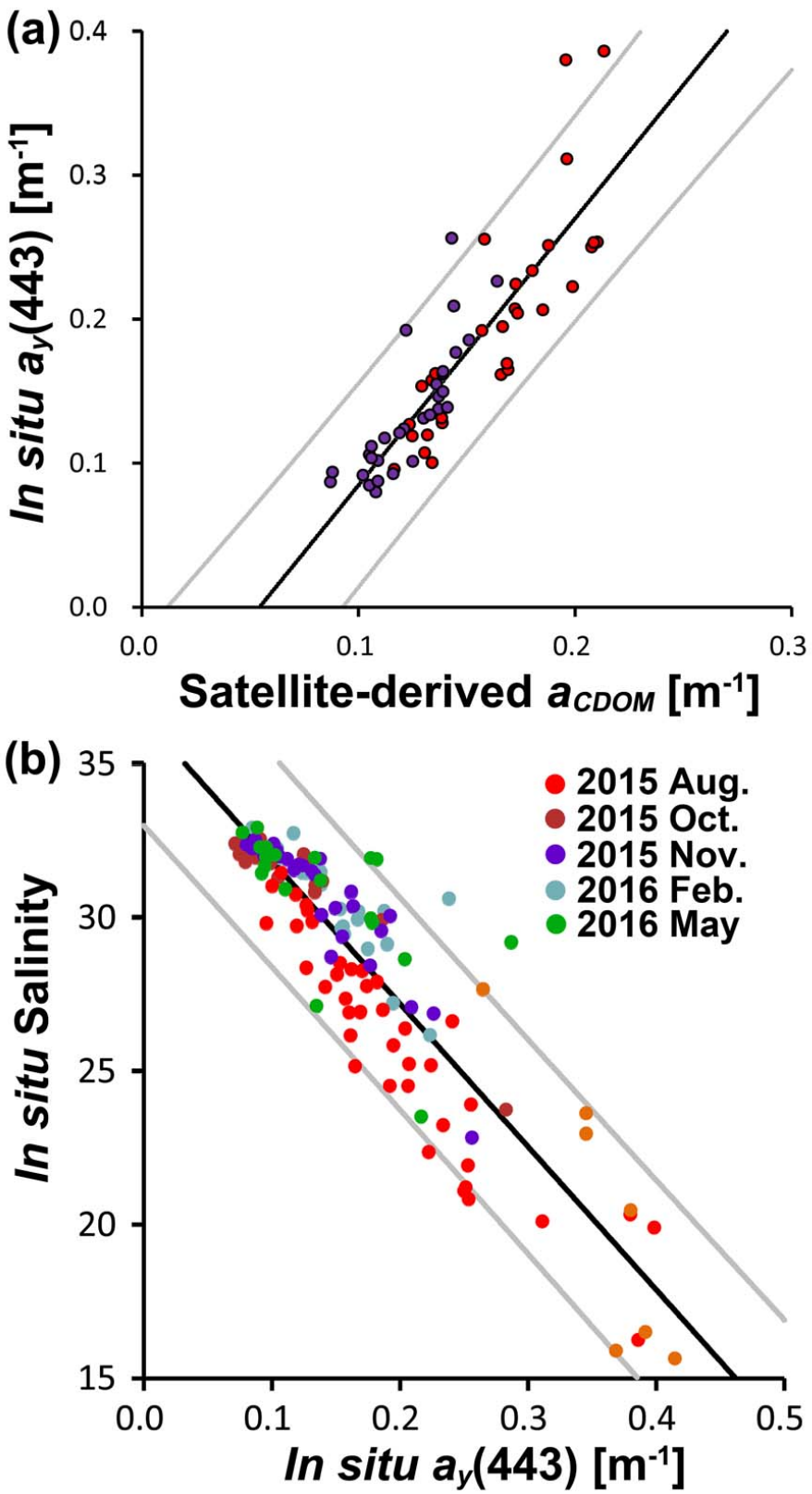

Figure 5 (a) Scatter plot comparing satellite-derived a_{CDOM} and *in situ* (observed) $a_y(443)$ (m^{-1}) data in match-up periods from 3–5 August and 2–4 November 2015. (b) Scatter plot showing *in situ* $a_y(443)$ (m^{-1}) and *in situ* sea surface salinity in summer (August 2015), fall (October, and November 2015), winter (February 2016) and spring (May 2016). Gray lines represent the 95% prediction interval.

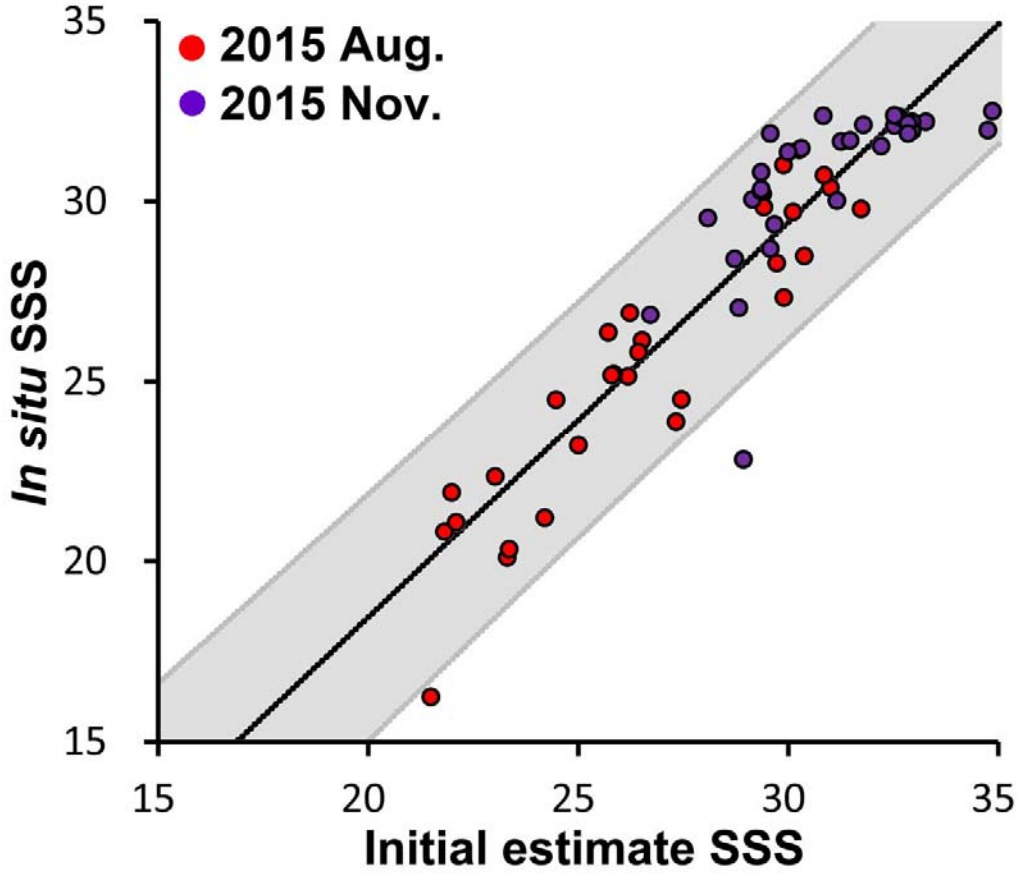

Figure 6 Comparison of satellite-derived and observed (*in situ*) sea surface salinity. Gray lines and areas represent the 95% prediction interval.

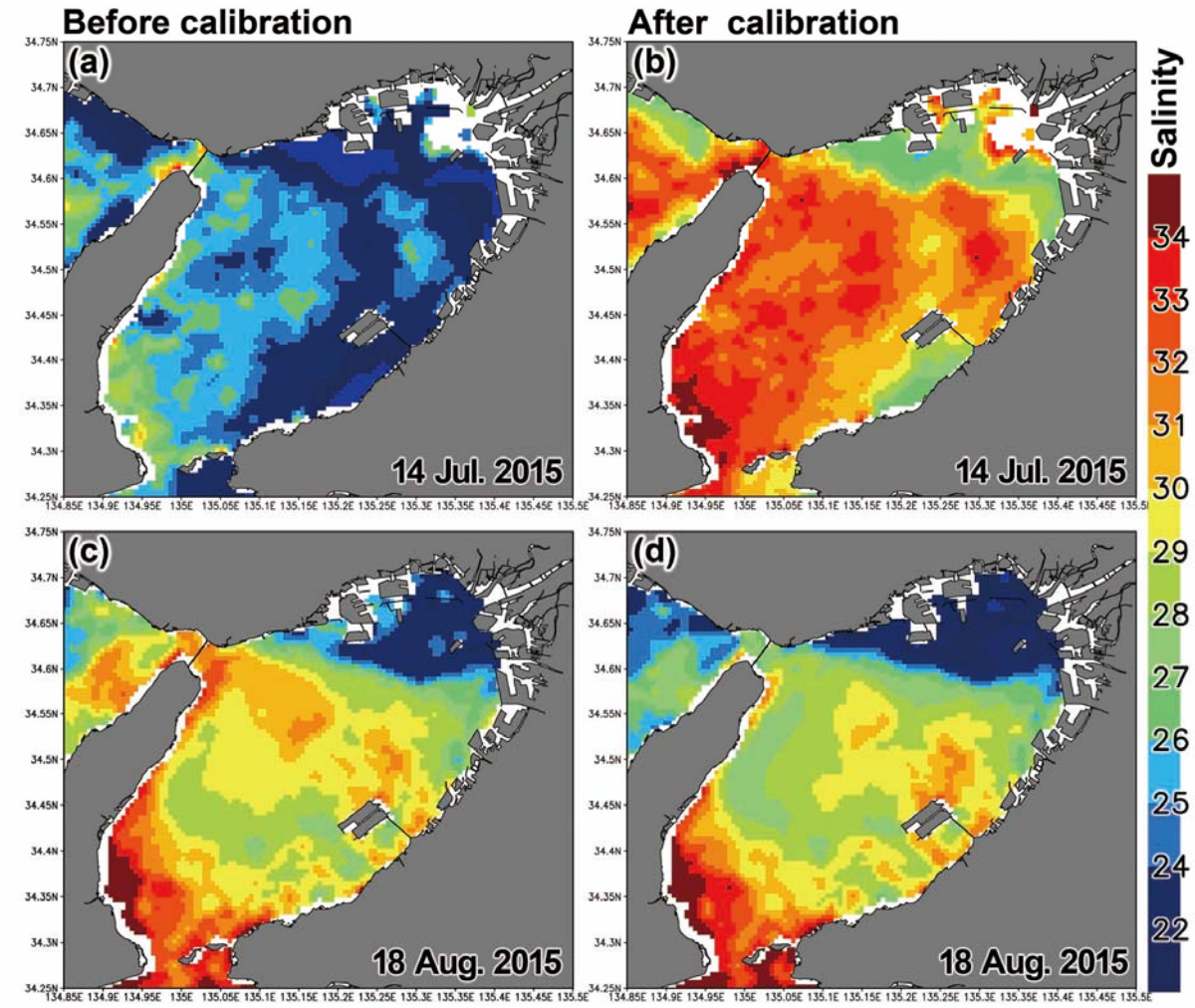

Figure 7 Maps of satellite-derived sea surface salinity from the initial estimate before calibration (a and c) and final estimate after calibration (b and d) on 14 July and 18 August, 2015.

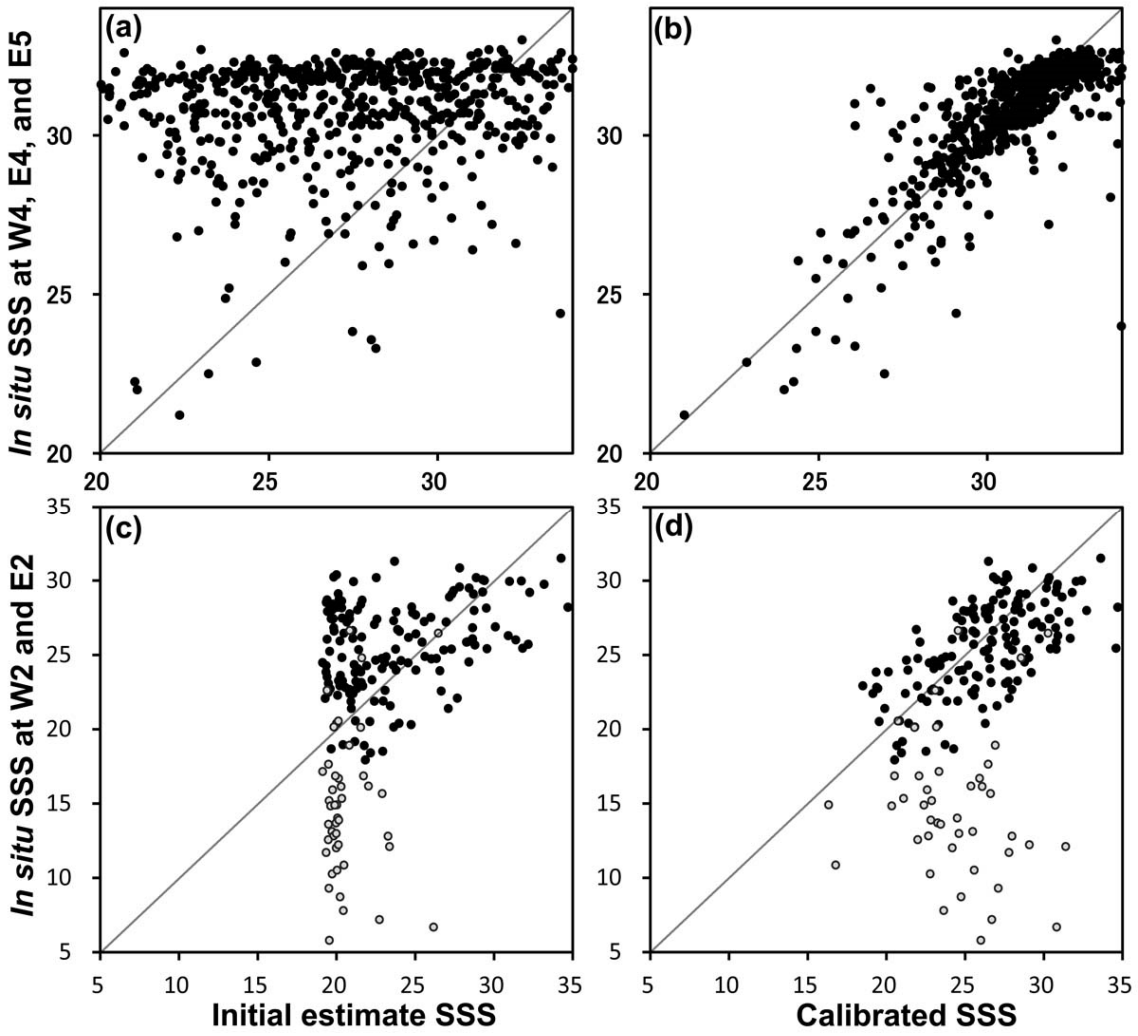

Figure 8 Comparison of initial estimates (left panels) and calibrated values (right panels) of sea surface salinity. *In situ* salinity, used in the upper and lower panels, was observed at the western offshore stations (W4, E4, and E5: red rectangles in Fig. 1) of OSAQAS and at the stations in the bay head (W2 and E2: blue rectangles), respectively. Plots were divided into a group with RMSE < 1.5 (black dots) and other data (open gray circles).

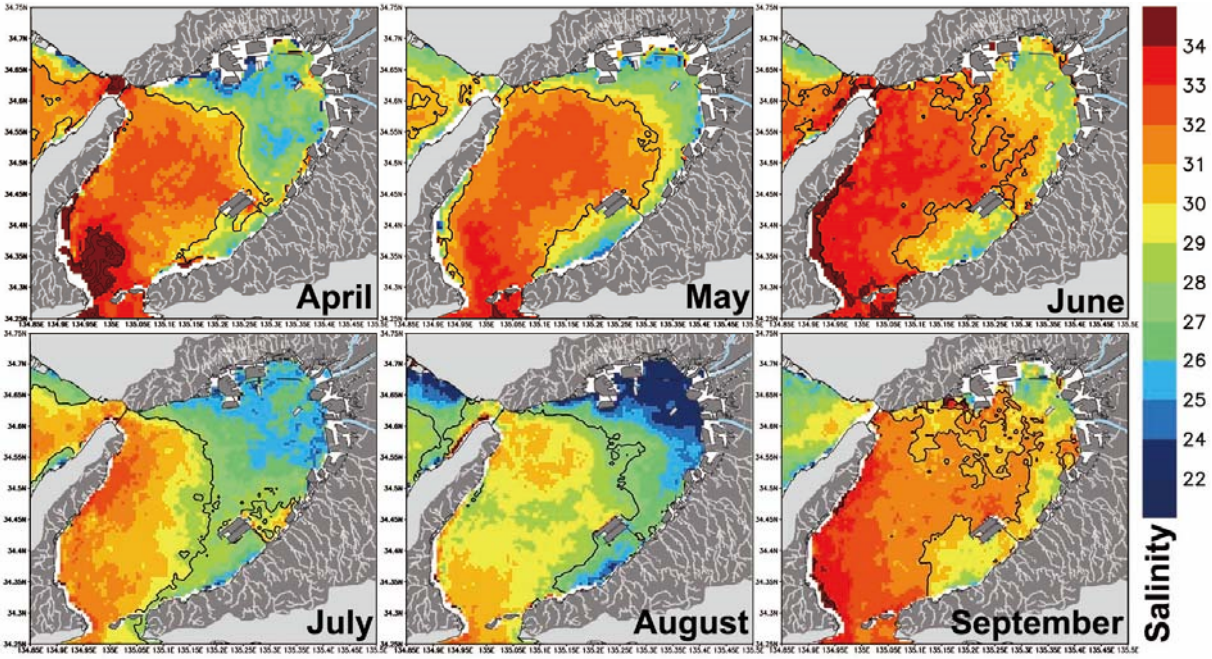

Figure 9 Maps of monthly mean, sea surface salinity collected by GOCI-COMS from April to September of the analysis period. Solid lines indicate the effective boundary of the plume. Pale blue lines in the watershed indicate river paths.

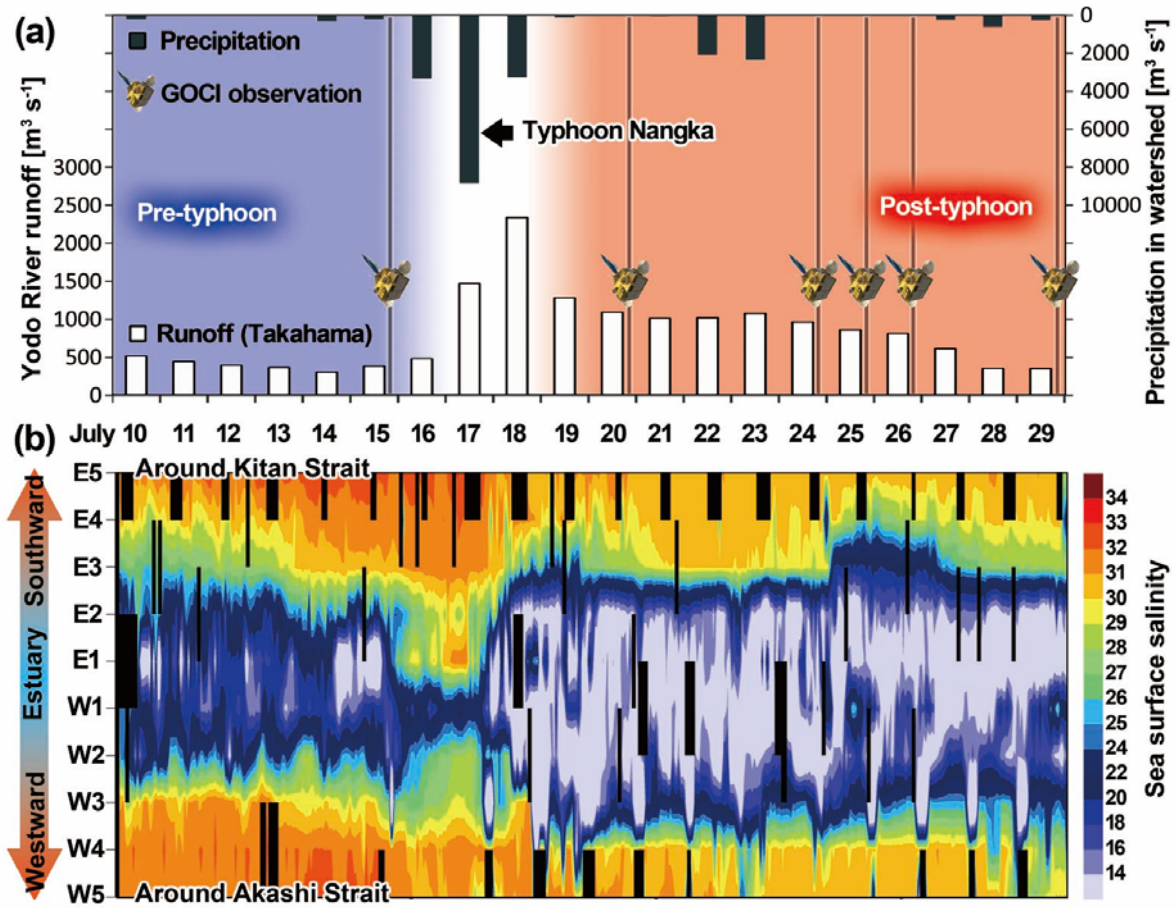

Figure 10 (a) Temporal variations in total daily precipitation (m^3 s^{-1}) estimated from AMeDAS data over the Yodo River watershed and runoff (m^3 s^{-1}) observed at Takahama (Fig. 1) during the pre-typhoon to post-typhoon period (10–29 July 2015). Solid lines indicate days for which satellite data were available. (b) Hovmöller diagrams of hourly nearshore sea surface salinity along the coast of the bay from 10–29 July 2015. The ten letter and number combinations (E1-E5 and W1-W5) correspond to the OSAQAS stations (Fig. 1). Stations E1 and W1, as shown on the vertical axis, are located in the estuaries of the Yodo and Yamato Rivers, respectively. Black rectangles in the diagram indicate missing data.

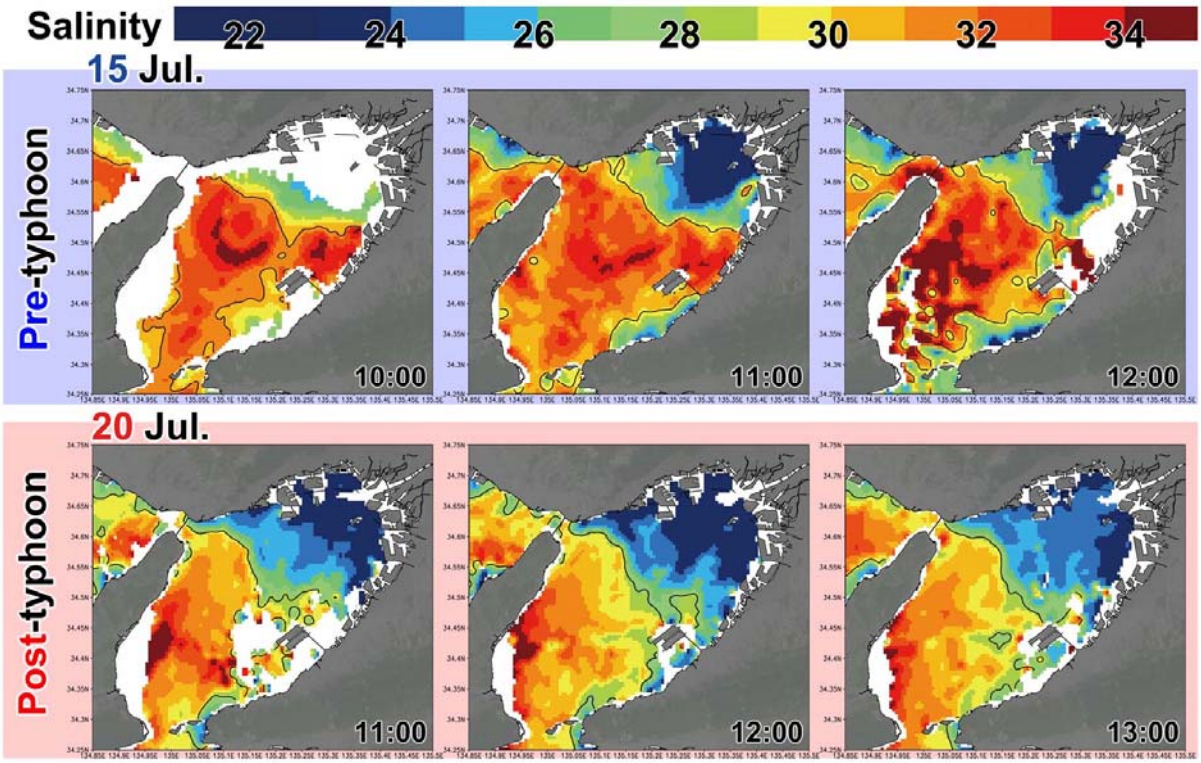

Figure 11 Hourly maps of sea surface salinity derived from GOCI-COMS in the pre-typhoon (15 July 2015) and post-typhoon (20 July 2015) periods. Solid lines indicate the effective boundary of the plume.

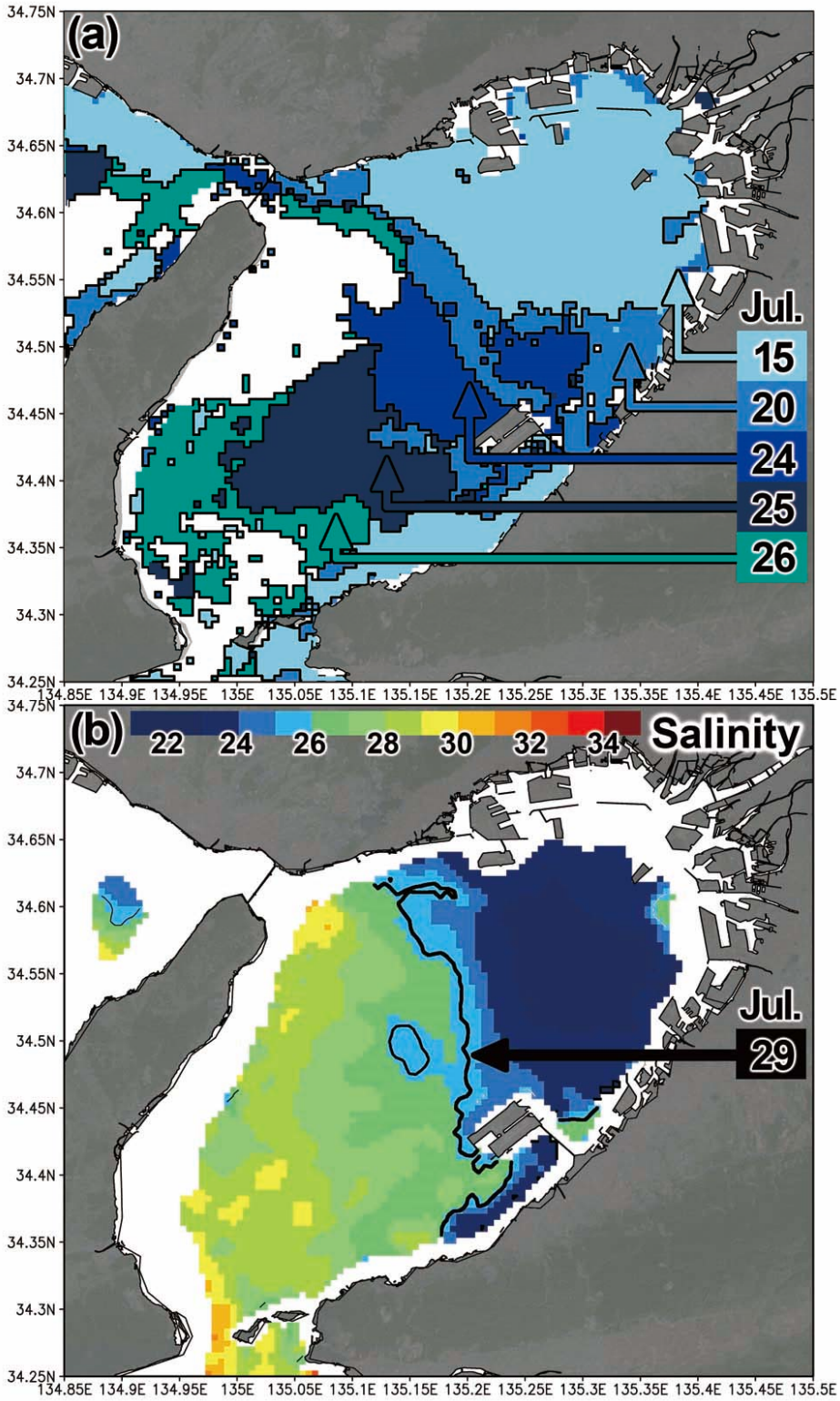

Figure 12 (a) Temporal variation of the effective boundary of the plume from 15 to 26 July 2015. (b) Map of sea surface salinity and the effective boundary of the plume (solid line) on 29 July 2015.

Table 1 Dates of observations conducted aboard the R/V Osaka (Marine Fisheries Research Center, Research Institute of Environment, Agriculture and Fisheries, Osaka Prefectural Government; MFRC-OPG) and the R/V Hakuo-Maru (Faculty of Maritime Sciences, Kobe University; FMS-KU).

Year	MFRC-OPG	FMS-KU
2015	August 3-4	August 4
	October 5-6	
	November 2 and 4	November 10
2016	February 1 and 3	
	May 9 and 12	

Appendix

A1. Estimation accuracy of offset maps

The accuracy of the offsets in procedure (6) (Fig. 2) was investigated to determine the effectiveness of using offsets in estimations using satellite-derived sea surface salinity (SSS) maps. The offset maps were used to improve the estimation accuracy of satellite-derived SSS maps using matchup data of the satellite-derived and *in situ* SSS at three representative Observing System for Aquatic Quality at Automated Stations (OSAQAS) observational stations (Fig. 1) based on Gaussian inter/extrapolation.

We first describe the temporal variation in the *in situ* SSS data at the three stations (Fig. A1) to evaluate the magnitude of the diurnal variation in the SSS. The temporal variations in the 1-day running mean SSS (black dots) at each station indicate that the SSS fluctuated around 31.6, with a small amplitude in April–June. The daily mean standard deviation (SD) was small throughout this period, although episodic increases in SD were evident. The average SD for the period was 0.88 less than the root mean square error (RMSE; 1.587) of the empirical formula, Eq. (1), used to estimate satellite-derived SSS from the satellite-derived a_{CDOM}(absorption coefficient of colored dissolved organic matter). This suggests that the small diurnal variation had an insignificant effect on the calibration of the SSS map.

In contrast, in July–August, when discharge from the Yodo River increased, the magnitude of the temporal variation increased (1-day running mean SD = 1.91). A marked dispersion in the hourly raw data (red dots) is evident in July–August. Comparing the temporal variations between May and July (Fig. A2), the dominant SD was obtained from the middle to end of July, indicating a larger diurnal variation. The diurnal variation might be induced by wind- and/or tidal-driven advection of a salinity front or river plumes induced by large river discharges. The large diurnal variation in the large discharge or flood period might affect the accuracy of the offset map and hence estimation of the daily mean SSS map.

Figure A3 shows the hourly offset map for 9:00–16:00 on 14 July 2015, when the offset values were significantly larger than those on other dates. The initial estimation of the hourly SSS map was modified by the hourly offset map. The horizontal contrasts of the offset values were within approximately 1.5 in the hourly maps. These contrasts were comparable to the RMSE of the empirical formula, Eq. (1). These results suggest that the horizontal patterns of the offset maps were ineffective with large-scale contrasts or distributions of the SSS maps. Fig. A3 shows that the temporal variation in the offset values in Osaka Bay ranged from 3 to 7. However, the *in situ* SSS data on 14 July exhibited a small range (32.4–31.5) at all three observational stations (e.g. Fig. A2), and their diurnal variations were also small (0.1–1). These results suggest that the range of offset values was largely determined by the temporal variation and/or errors in

the satellite-derived a_{CDOM}. Even if there is a large diurnal variation in the offset map, the daily mean map of the calibrated SSS is robust as long as the diurnal variation in the *in situ* SSS is smaller than the RMSE of Eq. (1).

We investigated the dependency of the offsets on the satellite-derived SSS maps. The offset maps were determined using a horizontal scale of the influence radius (r_G=20 km) of Gaussian inter/extrapolation and/or the number of matchup data at the three observational stations. We produced experimental SSS maps for cases using the matchup data at one or two stations, assuming that the missing data were the result of cloud cover or sensor malfunction, and for cases using the larger or smaller influence radius of Gaussian inter/extrapolation.

Figure A4 shows the daily mean satellite-derived SSS on 14 July after calibration (upper panel) and offset maps (lower panel) in the control case (CR) using all matchup data at the three stations and the influence Gaussian radius (r_G=20 km), and the six cases using one or two matchup data sets. The horizontal pattern of the SSS map was calibrated using all matchup data at the three stations (Fig. 7a and 7b). The CR was similar to the patterns of the other SSS maps in each case, although the absolute values of the SSS in each map differed slightly. This indicates that the spatial pattern of the SSS map was not sensitive to missing data at one or two stations or selection of the observational sites. The area-averaged offset value in Osaka Bay was 5.4 in the daily offset map for the CR. The range of daily area-averaged values in each daily offset map was 4.8–6.4, and the difference between the highest and lowest values (1.6) was comparable to the RMSE of the empirical formula, Eq. (1). This suggests that the effect of the offset on the accuracy of the SSS map did not depend significantly on the selection of observational sites; i.e., the daily mean offset map was robust even if one or two matchup data sets were missing. One matchup data set significantly improved the SSS map if one reliable time-series data set was derived at a fixed observation station.

To evaluate the temporal robustness of the daily mean offset map, we examined the temporal variations in the daily mean area-averaged offset values in each case for the period April–September 2015 (Fig. A5). The upper panel shows that the temporal variations in the offset values in the CR and three cases using smaller- and larger-influence Gaussian radii (r_G=5, 10, and 30 km) showed no significant difference. This indicates that the horizontal scale of the Gaussian radius was insensitive provided that the scale was smaller than the bay width (~30 km). The temporal variations in the cases using one and two matchup data sets were largely similar to the CR. However, larger differences among these cases was visible on 20 July, 18–24 August, and 2 September, when large river discharges were observed following typhoons, and were caused by salinity differences among the stations; e.g., the salinity difference was 2.3 calculated from in situ data on 20 July, which was attributed to the large river plume covering one or two stations. The differences in a case using only one matchup data set tended to be larger than those

in a case using two data sets. This suggests that during these periods we might derive multiple estimations or "multiple solutions" from the satellite-derived SSS map calibrated by the offset map depending on the number of missing data.

To evaluate data accuracy based on the temporal variation in the offset, we calculated the temporal variation in the daily anomaly for nine cases with reference to the offset value of the CR and the daily SD using the anomaly in each case (Fig. A6). The SD was larger than the RMSE of the empirical formula, Eq. (1), for SD = 4.3 on 20 July, SD = 1.6–2.0 on 18–24 August, and SD = 1.8 on 2 September. These larger SD values indicate that missing matchup data might produce larger errors in the SSS calibration using the offset map.

A2. Seasonality of the estimation formula of SSS from satellite-derived a_{CDOM}

We examined the seasonality of the estimation formula of SSS from a_{CDOM} data, because significant seasonal variation in the slope and interception of the formula may reduce the accuracy of the initial estimation of SSS. Significant differences in the slopes and interceptions among months were evaluated using the statistical t-test.

We evaluated the significant differences in the slopes and interceptions of regression lines derived by *in situ* SSS and *in situ* $a_y(443)$ data between the months of August and November 2015 under the null hypothesis in a two-sided t-test at the 99% confidence level. Fig. A7 shows two regression lines based on the data samples from the two months. We derived the slope (a_8 = −44.96) and interception (b_8 = 34.75) of the regression lines in August and November (a_{11} = −43.89, and b_{11} = 36.62) and calculated two t-values for the differences in the slopes ($t_a = 0.19$) and the interceptions ($t_b = 0.33$) between the two months. The 99% quantile in Student's t-test was 2.52 with 66 degrees of freedom calculated using the sample data numbers, indicating that there was no significant difference in the interceptions or slopes between August and November 2015.

For all data samples from the *in situ* SSS and $a_y(443)$ derived for each pair of months, we calculated each t-value between two data groups among August, October, November, February, and May. Table A1 shows that the 99% quantile in a two-sided t-test ranged from 2.65 to 2.73, with a range of degrees of freedom of 35–66, calculated using the sample data numbers. Therefore, no significant difference was found in any interception or slope at the 99% confidence level, which implies that there was no significant seasonality in the estimation formula. However, two large t-values were found for the slopes derived using the data groups for May–August and May–November. Similar to the slopes, these large t-values may be attributable to the a_{CDOM} and SSS data derived after the flood event in early May when a substantial river plume was formed by the large discharge from the Yodo River caused by the

high levels of precipitation on 9–12 May, 2016.

In a similar fashion to the t-test for the *in situ* SSS and a_{CDOM} data, we evaluated the significant differences for the slopes and interceptions of the regression lines derived from the *in situ* $a_y(443)$ and satellite-derived a_{CDOM} data between the months of August and November, 2015 as shown in Fig. 5a. We derived two regression lines based on the data samples in the two months and calculated their slope ($c_8 = 2.11$) and interception ($d_8 = -0.15$) in August and November ($c_{11} = 1.94$, and $d_{11} = -0.10$), as well as two t-values for the differences in the slopes ($t_c = 0.45$) and the interceptions ($t_d = 0.11$) between the two months. The 99% quantile in Student's t-test was 2.67 with 56 degrees of freedom, calculated using the sample data numbers. This indicates that there was no significant difference in the interceptions or slopes between the two months. However, it was difficult to examine the seasonality of regression between the *in situ* and satellite-derived a_{CDOM} data, because the matchup data for the *in situ* $a_y(443)$ and satellite-derived a_{CDOM} were derived only for August and November. Based on these statistical results, the satellite-derived a_{CDOM} can be corrected using procedure (2), as shown in Fig. 2.

Table A1. T-values for slopes and interceptions for each pair months in pale blue and red boxes (lower and upper triangular elements), respectively. The slopes and interceptions were calculated by two data samples from the *in situ* SSS and $a_y(443)$ in each month. Subsequently, t-values with the 99% quantile in a two-sided t-test were derived for each pair of months among August, October, November, February, and May. Dark blue boxes indicate t-value larger than 2.0.

	Aug.	Oct.	Nov.	Feb.	May
Aug.		0.075	0.327	0.100	0.069
Oct.	1.521		0.271	0.049	0.113
Nov.	0.186	1.714		0.154	0.304
Feb.	1.349	0.187	1.476		0.124
May	2.654	1.123	2.383	0.802	

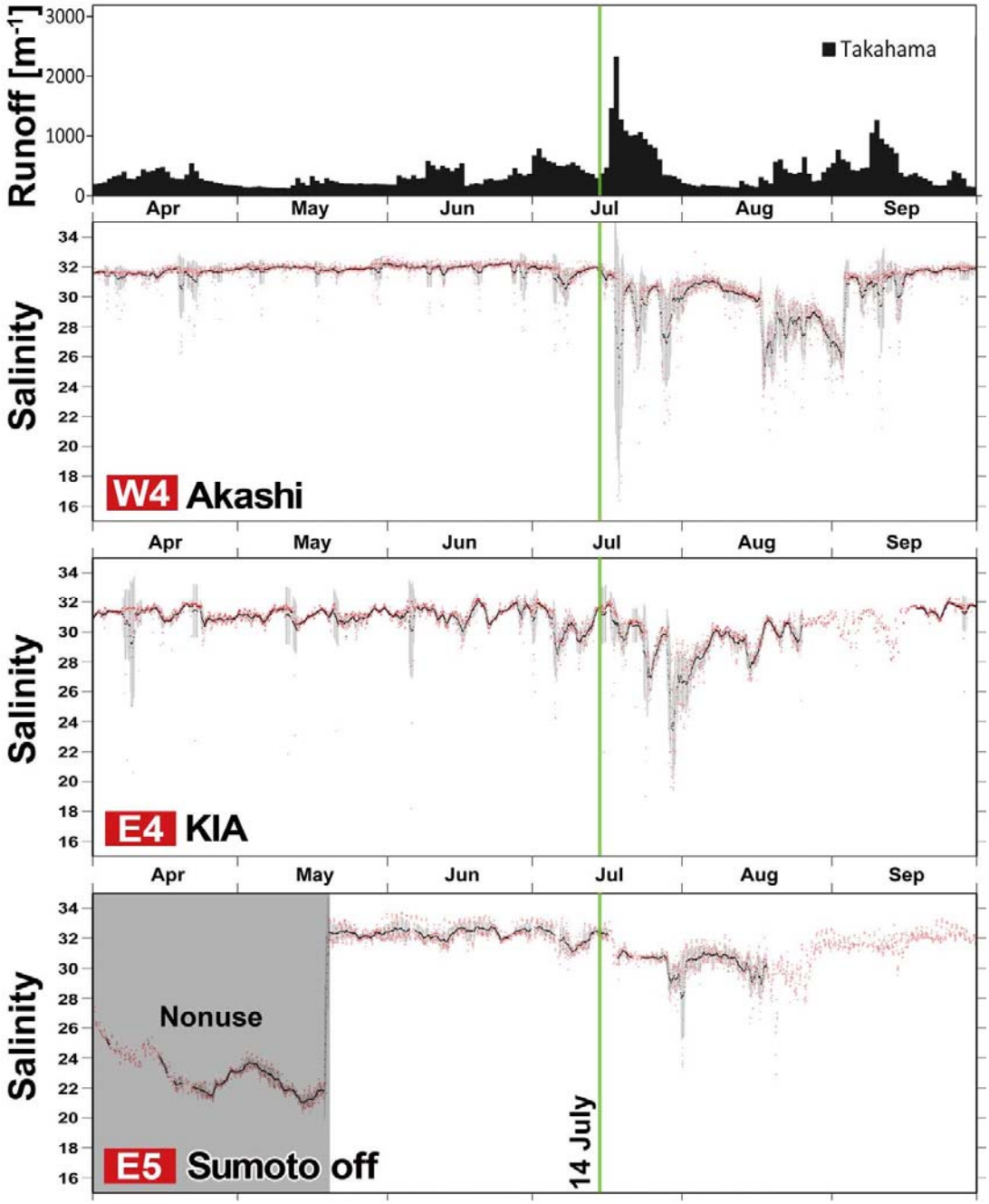

Fig. A1. Temporal variations in total daily runoff (m^3 s^{-1}) observed at Takahama (Fig. 1) in April–September 2015 (upper panel) and *in situ* SSS at the three OSAQAS observational stations (Fig. 1) used for the calibration of the SSS maps. Black and red dots indicate the raw and 1-day running-mean SSS data, respectively. The gray shaded areas represent the 1-day mean standard deviation calculated from hourly data for 1 day. The solid green line indicates the date of 14 July, which was used to investigate the dependency of the offsets on the satellite-derived SSS maps.

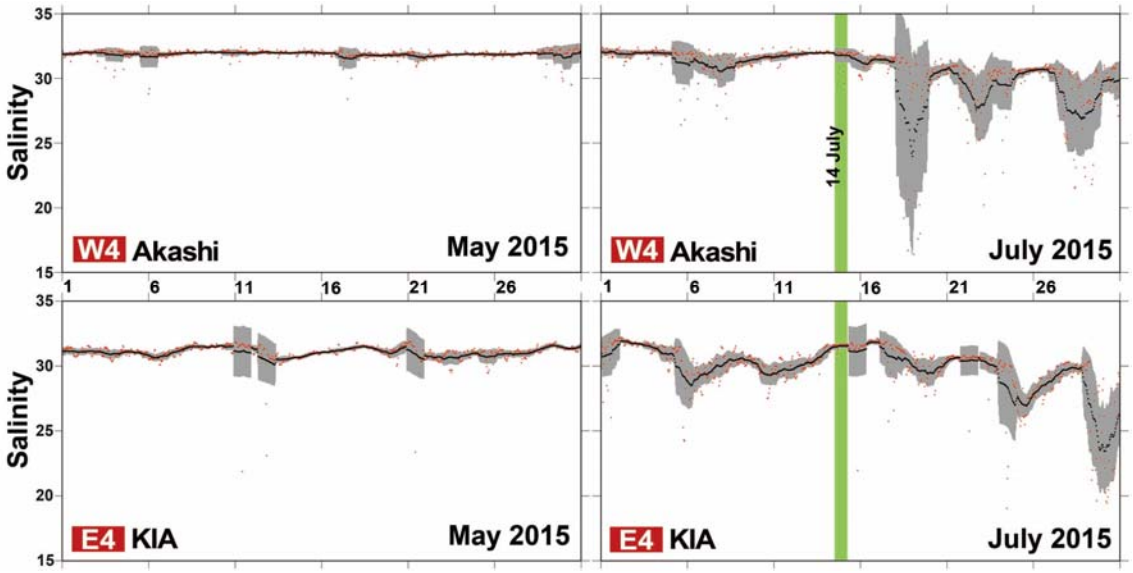

Fig. A2. Temporal variations in *in situ* SSS at the two OSAQAS observational stations (Akashi and KIA) (Fig. 1) in May and July 2015. Black and red dots indicate the raw and 1-day running mean SSS data, respectively. The gray shaded areas represent the 1-day mean standard deviation calculated from hourly data for 1 day. The solid green bar indicates the date of on 14 July, which was used to investigate the dependency of the offsets on the satellite-derived SSS maps.

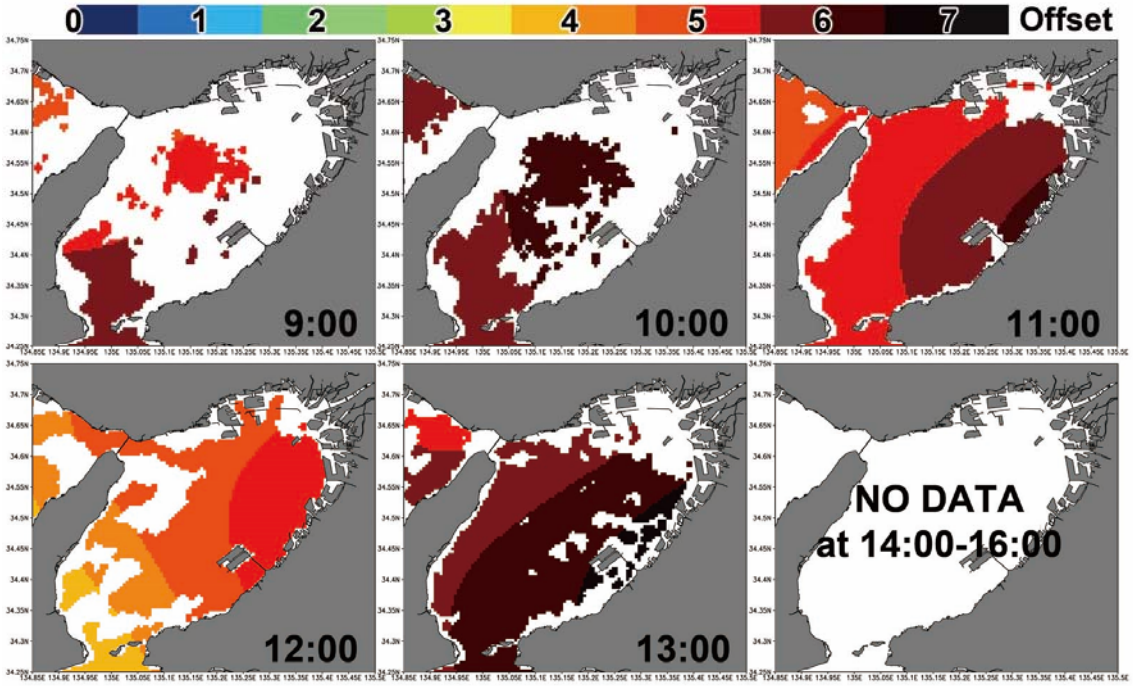

Fig. A3. Hourly offset maps at 9:00–16:00 on 14 July 2015.

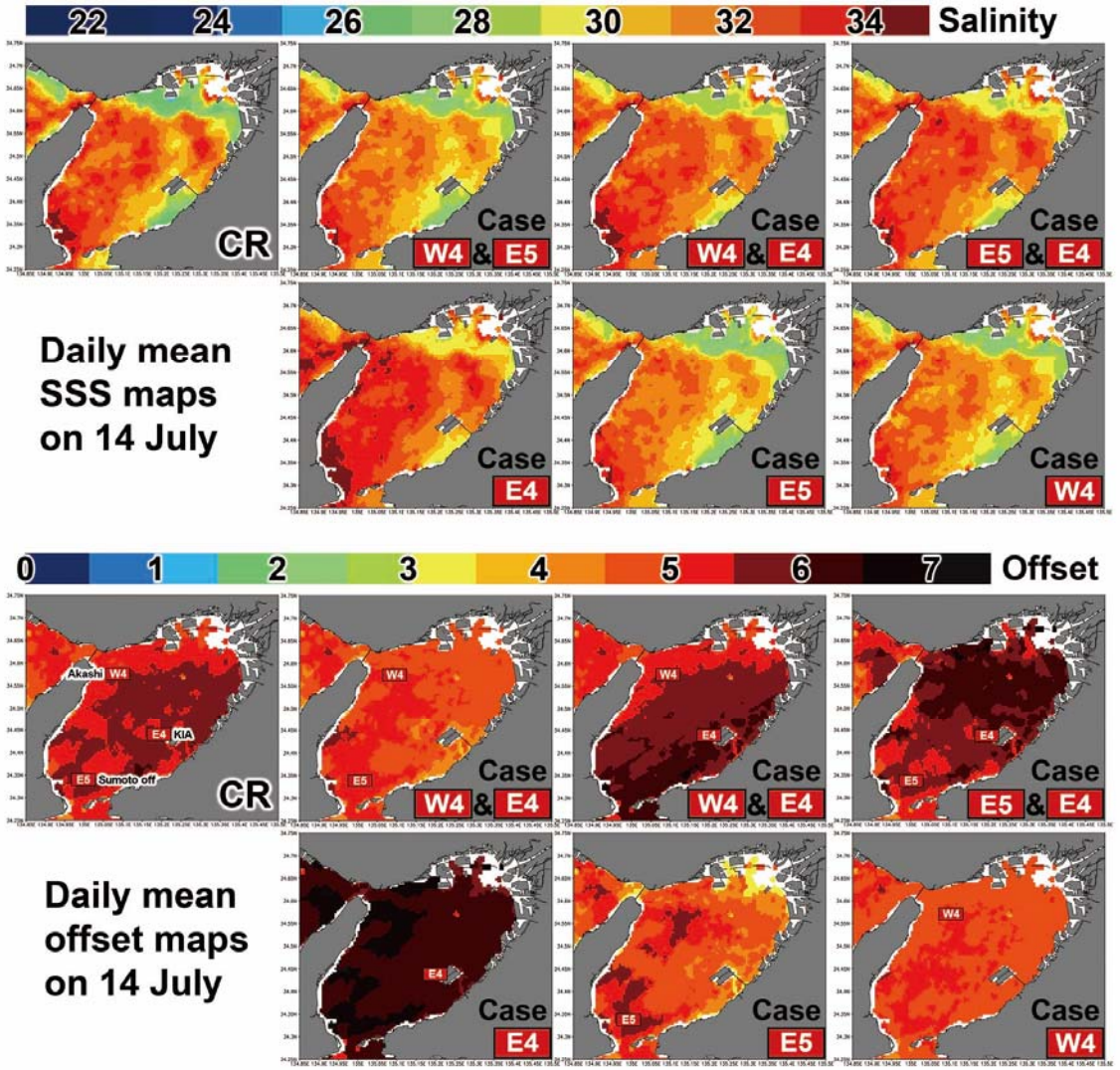

Fig. A4. Daily mean satellite-derived SSS on 14 July 2015 after calibration (upper panels), offset maps (lower panels) for the control using three matchup data sets, and six cases using one or two matchup data sets among three OSAQAS observational stations.

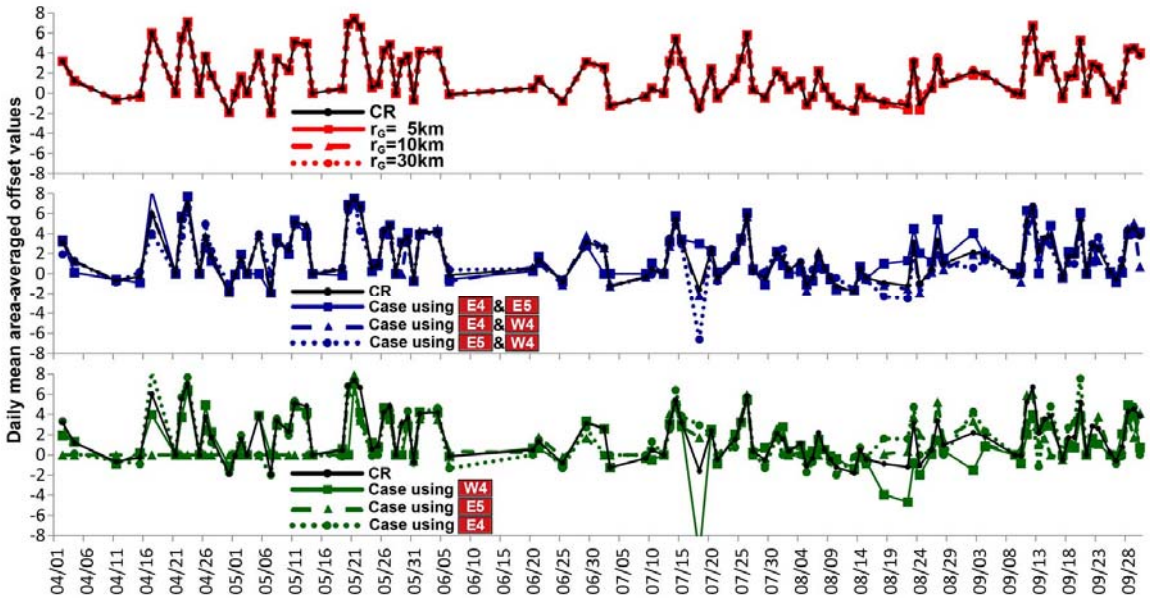

Fig. A5. Temporal variations in the daily mean area-averaged offset values for the control and nine cases in April–September 2015. Temporal variations in the offset values (upper panel) for the control and three cases (red) using smaller- and larger-influence Gaussian radii (r_G=5, 10, and 30 km): (upper panel) for control and three cases (blue) using two matchup data sets and (lower panel) for control and three cases (green) using only one matchup data set.

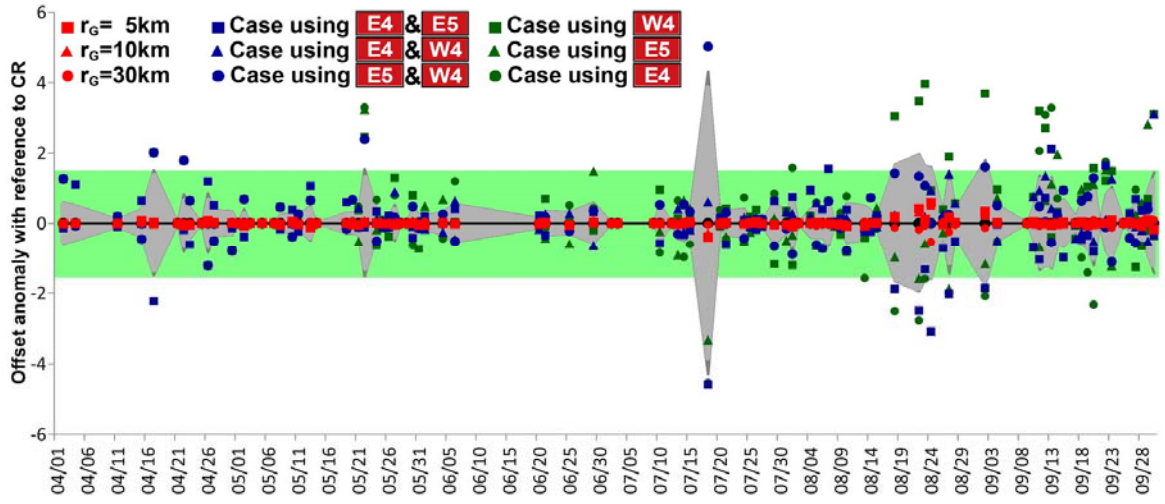

Fig. A6. Temporal variations in the anomaly of the daily mean area-averaged offset values for the control and nine cases in April–September 2015. Red squares, triangles, and circles indicate three cases using smaller- and larger-influence Gaussian radii (r_G=5, 10, and 30 km), blue symbols indicate three cases using two matchup data sets, and green symbols indicate three cases using only one matchup data set. Gray shaded areas represent the daily mean standard deviations calculated using the data derived from the control and nine cases. The green shaded area indicates a range smaller than the RMSE of the empirical formula, Eq. (1).

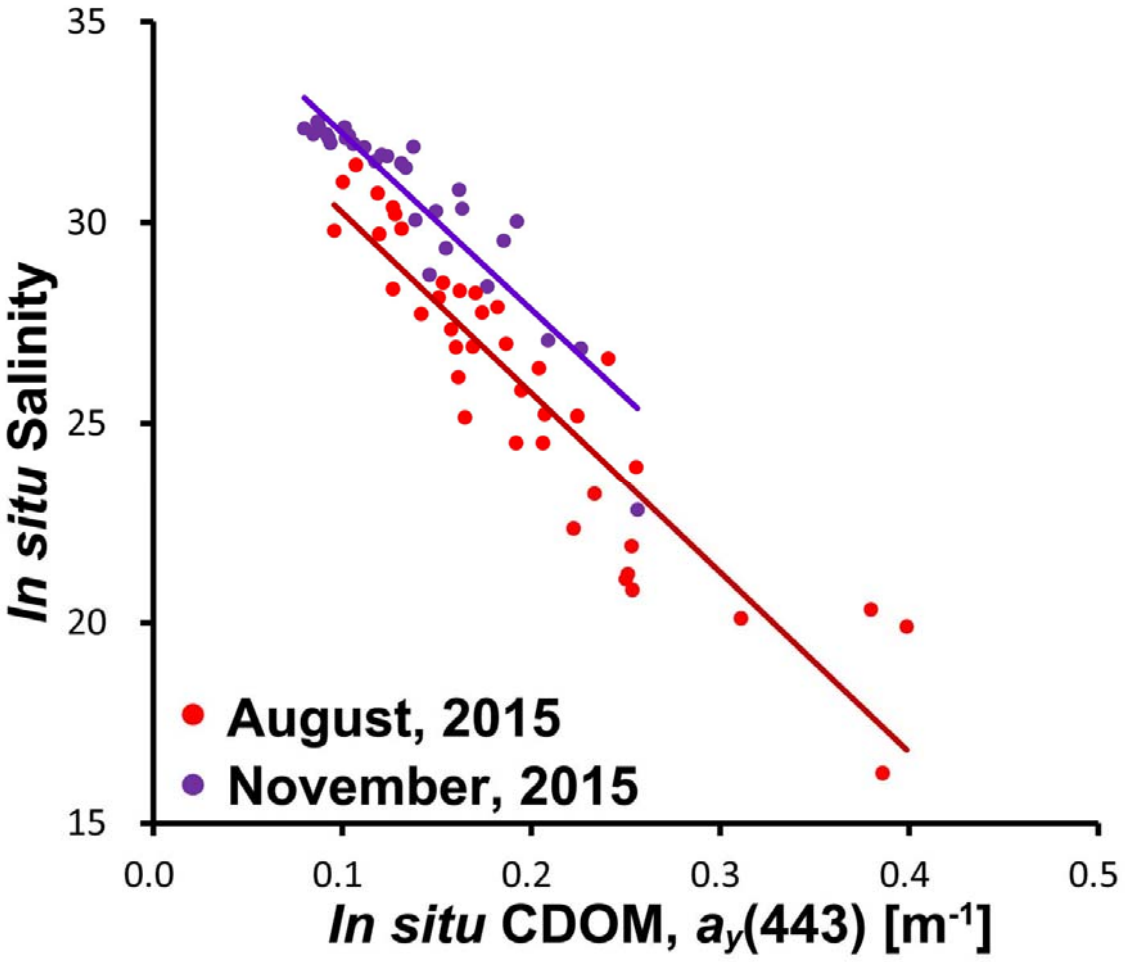

Fig. A7. Scatter plot comparing satellite-derived a_{CDOM} (m^{-1}) and *in situ* (observed) SSS data in match-up periods from 3–5 August (red) and 2–4 November 2015 (purple). Red and purple lines indicate regression lines.